Construction and Building Materials 457 (2024) 139147

Contents lists available at ScienceDirect

Construction and Building Materials

journal homepage: www.elsevier.com/locate/conbuildmat

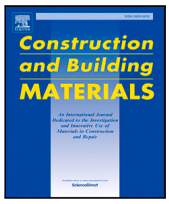

Multiaxial characterisation and nonlinear thermoviscoelastic isotropic and orthotropic constitutive models of ETFE membranes

Alessandro Comitti [a], Federico Bosi [a,b,*]

[a] Department of Mechanical Engineering, University College London, Torrington Place, WC1E 7JE, London, UK
[b] Department of Innovative Technologies, University of Applied Sciences and Arts of Southern Switzerland, 6962 Lugano Viganello, Switzerland

ARTICLE INFO

Dataset link: github.com/fbosi/ETFE-NLVE-model

Keywords:
Lightweight construction
Tensile structures
Viscoelasticity
Polymers
Ethylene tetrafluoroethylene

ABSTRACT

Ethylene-tetra-fluoroethylene (ETFE) is a stiff and ductile polymer widely employed in cladding elements for roofs and façades, formed in pneumatic cushions or tensioned foils. The material's high thermoviscoelastic effects require a comprehensive time and temperature-dependent multiaxial characterisation and accurate constitutive model to foster the design of lightweight ETFE tensioned construction and their standards. A multiaxial experimental campaign is performed to assess the material response in a wide range of temperatures, from −20°C to 60°C, strain rates, from 0.01%/s to 1%/s, and mechanical loading conditions typical of ETFE buildings. Uniaxial and biaxial bulge tests on circular and elliptical samples are carried out to assess constant strain rates, pressure rates and temperatures, unloading, cyclic, creep and relaxation conditions until the material yield point. Two nonlinear thermoviscoelastic plane stress constitutive models, one isotropic and one orthotropic, are developed using the Eyring stress shift factor to capture material nonlinearities, in the framework of the Boltzmann and the time–temperature superposition principles. A freezing of the Eyring shift factor during unloading has been introduced to represent ETFE relaxation and cyclic conditions. The numerical implementation of the consecutive models within finite element software is made available open source and has enabled the their validation on independently acquired data. The results show high accuracy between measurements and predictions from both isotropic and orthotropic formulations, thus paving the way for their use in structural design to capture highly nonlinear time and thermal effects, such as multiaxial prestress loss after installation or creep caused by variable loads.

1. Introduction

Ethylene-tetra-fluoroethylene (ETFE) is a well-known material in the field of architectural membrane structures, as it is widely used in high-profile constructions to cover large spans roofs or facades, with a highly transparent envelope able to withstand external thermo-mechanical loads using a low amount of material [1]. The light transmission properties and the versatility of ETFE tensile structures raise significant interest in architectural applications. Moreover, the lightness of ETFE-based tension structures is advantageous when targeting sustainable development in the building industry. A lightweight envelope often results in lighter structures, as less weight needs to be supported and carried to the foundation [2,3].

ETFE is a semi-crystalline polymer with a degree of crystallinity of 30%–40% depending on the manufacturer [4]. ETFE exhibits a viscoelastoplastic response, highly dependent on the temperature and the loading profile in time. Several scientific contributions discussed the effects of the variation of those variables starting from uniaxial tensile tests, qualitatively agreeing that temperature has a predominant effect on the material's stiffness and yield point when compared to the strain rate, in the application range tested in the literature (0 °C to 50 °C, 0.1 to 200%/s) [5–9] . However, some uncertainty and variation in the results exist due to different foil manufacturers and thicknesses [4], specimen sizes and shapes (dumbbell or rectangular), strains measuring equipment (optical measurements or nominal calculations from the cross-head displacement of the testing machines) and data analysis. Compared with uniaxial measurements, the characterisation and modelling of the biaxial behaviour of ETFE has received less attention thus far, despite being the main stress state of an ETFE foil installed on a building envelope. Galliot and Luchsinger [8] performed uniaxial and biaxial tests on a 250 μm ET-6235Z foil from Nowofol, using both planar cruciform and circular diaphragm inflation tests. The authors found good agreement between all the procedures when comparing the uniaxial and biaxial equivalent stress–strain plots. More recently, Surholt et al. [10] performed a comprehensive characterisation on

* Corresponding author at: Department of Mechanical Engineering, University College London, Torrington Place, WC1E 7JE, London, UK.
E-mail addresses: f.bosi@ucl.ac.uk, federico.bosi@supsi.ch (F. Bosi).

https://doi.org/10.1016/j.conbuildmat.2024.139147
Received 8 September 2024; Received in revised form 17 October 2024; Accepted 9 November 2024
Available online 3 December 2024

ETFE through circular inflation and cruciform biaxial tests to determine the material stiffness, confirming the observation made by Galliot and Luchsinger and showing comparable results in uniaxial and biaxial procedures until the yield point, caused by yielding of the amorphous phase [4]. However, the equivalent uniaxial and biaxial behaviour differs in the viscoplastic regime, even though it is acknowledged that different test strain rates might have contributed to enhancing the discrepancies. Although the strain rate does not drastically impact the mechanical response of the foils when uniaxially or biaxially loaded, especially before the yield point, the material's time effects are more pronounced in constant stress or strain conditions, where creep and relaxation behaviours arise, respectively. These effects are highly nonlinear on ETFE foils and depend on the stress level achieved by the material, as shown by Li and Wu [11] in their uniaxial creep-recovery tests, among the others [12,13]. Such response is also confirmed in the biaxial creep campaign of Surholt et al. [14], where uniaxial and biaxial planar creep tests are carried out at 8 and 12 MPa for three different ETFE foil manufacturers.

Furthermore, to the best of the authors' knowledge, no contributions in the literature have investigated in depth the stress relaxation of ETFE, although such a loading profile is fundamental for the installation of stretched foils. A few tests were performed at ambient temperature and various stress levels [15,16] while some biaxial relaxation procedures were performed while changing the temperature [17]. Another rarely investigated property of the foils is their thermal expansion [18], hardly found in the literature except from a recent contribution of Sun et al. [19] on rectangular specimens of golden colour, quite unusual for ETFE foils discussed so far. They determined the thermal expansion properties from 25 °C to 140 °C, with a temperature ramp of 2 °C/min, using a thermal analyser and dilatometer to measure the in-plane and out-of-plane response, respectively. From their results, it is possible to notice that the in-plane values are generally one order of magnitude higher than the typical values for construction materials such as metals and concrete ($\approx 10^{-5}$). This highlights the crucial importance of the thermal strains when evaluating the overall behaviour of ETFE membranes and the necessity of their inclusion in the modelling.

Capturing altogether the time, temperature and stress-dependent effects in a constitutive law is a task that has seen many attempts in recent contributions, althought the existing models seldom include the thermal strains in their formulation. Some authors proposed using linear or nonlinear viscoelastic equations to fit individually experimental curves, mainly creep data [11,14,20]. However, different material parameters were determined for each stress level of the creep tests, thus lacking generalisation and viscoelastic validation to different conditions. Yoshino and Kato [21–24] performed a comprehensive material characterisation in uniaxial and biaxial conditions, and formulated a unified model built according to linear viscoelasticity. Moreover, the authors extended their model in the nonlinear domain through a custom stress function. However, their constitutive law was shown to be inaccurate when simulating experimental data that was not used to fit the model.

Achieving an accurate prediction of ETFE behaviour is crucial to practical applications and, ultimately, to fostering the use of lightweight tensile construction technologies in the building sector. The lack of regulation for their design reflects the gap in the literature, even in its most recent developments. The FprCEN/TS 19102:2023 [25], the most updated document containing design recommendations for ETFE structures, refers to the time-dependent behaviour in some of its sections, although not clarifying completely how to design for it. At the moment, the contributions in the literature do not provide any information on the relaxation behaviour of ETFE, present limited data on the thermal expansion behaviour of the foils and contain only isotropic constitutive models built on specific thermal and stress conditions. Therefore, the current research aims to provide a better understanding of ETFE behaviour and modelling to improve the current design practice by offering a reliable and powerful prediction tool. The focus is on viscoelastic region to avoid permanent strains of the foils, which are potentially dangerous because they can cause ponding and wind-induced fluttering [26]. The uniaxial tests employed to develop an orthotropic linear viscoelastic model [5] are here integrated with uniaxial relaxation, creep, cyclic and biaxial inflation and creep tests on circular and elliptical specimens, as well as thermal dilatation measurements, to develop, validate and numerically implement an isotropic and orthotropic nonlinear thermoviscoelastic constitutive models valid for a wide range of temperature, i.e. from −20 °C to 60 °C, and strain rate conditions, from 0.01%/s to 1%/s, typical of ETFE buildings.

The paper is organised as follows: Section 2 presents the tested material and the experimental campaign; Section 3 describes the modelling approach adopted to describe the linear and nonlinear viscoelastic responses, the formulation and its numerical implementation through a material subroutine; Section 4 shows the fitting and validation of the developed constitutive relations, comparing the isotropic and orthotropic model predictions with experimental measurements in a wide range of test conditions; Section 5 presents the discussion of the results achieved and some reflections on the model's applicability in the building sector, while Section 6 concludes the paper.

2. Thermomechanical characterisation

The experimental campaign was performed to characterise the nonlinear viscoelastic response of ETFE membranes in a wide range of temperatures, strain rates, and mechanical loading conditions (uniaxial, biaxial, creep, relaxation, cyclic) representative of building applications. The tests were performed on a 200 μm thick foil produced by Nowofol (ET6235Z), widely used in construction. The foil is obtained through the melting of ETFE granules, subsequently extruded in a film along an axis, denoted as machine direction (MD), while the orthogonal direction is called transverse direction (TD). The material is characterised both in MD and TD directions to assess its strain-dependent orthotropic response, as shown in Fig. 1 for representative uniaxial tensile tests at ambient temperature. The shapes selected for each test were laser cut to achieve high precision in specimen preparation. The tests were carried out using different experimental apparatus described in Section 2.1, while each test procedure is presented in Section 2.2. By analysing the first inflection point of ETFE stress–strain responses (Fig. 1), assumed as the yield point in the literature and by the authors' tests, the material yield strain was found to span between 2% and 2.8% depending on the temperature and strain rate. Hence, engineering quantities are considered throughout this paper for both the experimental data analysis and the subsequent constitutive modelling [6]. The results of the various experiments are presented in Section 4 alongside the predictions from the developed constitutive model, described in Section 3.

2.1. Experimental equipment

The setups used for the thermomechanical characterisation include a Dynamic Mechanical Analyser, a universal electromechanical testing machine and a custom biaxial inflation setup for circular and elliptical diaphragm tests. For each setup, the main components are described, together with the measurements recorded and how stresses and strains were obtained.

2.1.1. Dynamic mechanical analyser

A Dynamic Mechanical Analyser (Discovery DMA 850, TA Instruments) equipped with tensile clamps was used to carry out uniaxial creep and relaxation procedures. The machine can achieve the desired stress or strain level with a ramp of approximately 210 MPa/s, and record the data in time instants equally spaced on a logarithmic time scale, particularly convenient for the procedures investigated. The test temperature could be varied using the machine's thermal chamber

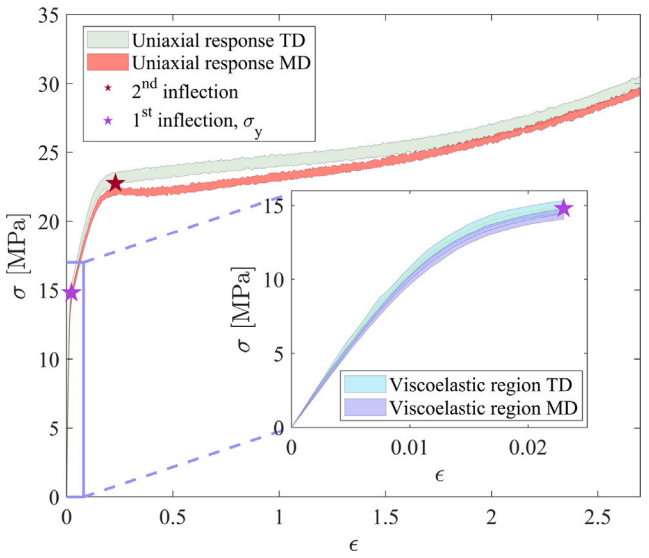

Fig. 1. Representative engineering stress–strain response for uniaxial tensile test of an ETFE foil at ambient temperature. The main plot also highlights the two characteristic inflection points, while the inset represents the viscoelastic domain, where the current work focuses. (For interpretation of the references to colour in this figure legend, the reader is referred to the web version of this article.)

and an external LN_2 dewar. The specimens were laser cut to a width of 5.5 mm and a length of ≈18 mm. The nominal uniaxial strain was extracted from the data log, considering the exact length of the specimen measured by the machine after the conditioning phases, i.e. temperature soaking. The nominal stresses were determined using the initial area of the specimen, calculated from the measurements obtained with an electronic calliper and an electronic micrometer.

2.1.2. Universal testing machine and digital image correlation

An Instron 5985 equipped with a 2530–500 N load cell and 2713-004 self-tightening roller grips was used. The temperature was controlled through a 3119-606 Instron environmental chamber cooled by LN_2, while a two-channel Omega HH801 A meter recorded the temperature in the vicinity of the specimens with two thermocouples type K. The engineering stress was computed from the force recorded by the load cell on the nominal area of the specimen.

The measurement of the kinematic fields (displacements, curvatures and strains) was performed using Digital Image Correlation (DIC) [27]. The stereo system comprised two digital cameras Basler acA2440 75 µm 5.0 MP, equipped with Schneider Kreuznach Xenoplan 1.9/35 mm lens. The images were acquired through VICSnap 9.0 (Correlated Solutions) and processed by VIC3D 8.0 (Correlated Solutions). The stereo system was calibrated by acquiring pictures of a calibration plate (14 × 10 dots grid, with a spacing of 7 mm) in different positions and tilt angles from the test reference plane. The goal was to obtain a calibration score lower than 0.03 pixels to achieve good accuracy, with a minimum of 30 images per camera. The specimens were laser cut according to the dimensions indicated in ASTM D412 (2021), type 'A' die [28]. Each specimen was spray painted with Rust-Oleum 330505 universal black paint (matte effect) to create a random speckle pattern. Preliminary analysis on uniaxial tensile tests showed that the paint has no influence on the measured mechanical response of ETFE. An external LED light was used to obtain adequate light conditions and enhance the contrast between the transparent specimen and the black speckles. To avoid the poor quality of the images caused by light reflection on the external glass of the environmental chamber, a custom aluminium frame equipped with a light-diffusing panel and adhesive strips of LED lights was placed behind the specimen. In the image post-processing phase, the correlation subset was 29 × 29 pixels, with a step size of 7 pixels and a filter size of 15 pixels [29].

2.1.3. Biaxial inflation rig

Inflation experiments have been conducted to characterise the material biaxial property across various temperatures and pressure rates. Two different shapes of the initially planar membrane were investigated to achieve different principal stress ratios at their apex once inflated. The custom biaxial inflation setup, shown in Fig. B.27, comprises a metallic box closed by a lid. The lids used have (i) a circular hole of 10 cm in diameter and (ii) an elliptical hole, with major and minor axis of 12 and 6 cm, respectively. The ETFE membranes were placed on top of the lid and clamped through a screwed-in metal ring, guaranteeing the boundaries' air-tightness around the hole. The box is equipped with a compressed air inlet and internal white LED lights.

During the tests, the box was placed between Instron 2501 compression platens in the universal testing machine setup described previously. This allowed the use of the environmental chamber for temperature conditions other than ambient. Analogously to the uniaxial tests described above, the temperature was monitored and recorded with two thermocouples and displacement, curvature and strain measurements were obtained with DIC. During the tests, pressurised air was imposed via a custom setup composed of an SMC ITV0030-3BS pressure regulator, an Omega DPG409-50 pressure gauge and a Correlated Solutions Data Acquisition DAQ-STD-8D. Through National Instruments (NI) Signal Express 2015 software, a ramping signal in the range 0–10 V was generated from the DAQ and input to the pressure regulator, which converted it into air pressure (0–0.345 MPa). The gauge recorded the chamber's pressure and input it into the DAQ as a voltage signal. NI Signal Express acquired this input, which Vic-Snap saved as a voltage at every image acquisition and converted to pressure.

The stress values in the membrane are determined in different ways. For both circular and elliptical shapes investigated, the most interesting point of stress extraction is the apex of the membrane, which shows the highest Von Mises stress and the principal stresses are aligned to the material directions, i.e. there is no shear stress. For circular tests, the almost perfect axisymmetric configuration of the inflated specimen and the approximation of material isotropy enable to calculate the apex's equibiaxial stress as $\sigma_{eqbiax} = \frac{pR}{2t}$, where p is the pressure, R is the mean radius of curvature and t represents the specimen thickness. For elliptical membranes, the non-axisymmetric deformed configuration prevented a direct calculation of the stresses. In this case, the data analysis procedure followed Suleman and Bosi [30] and, for each DIC picture acquired during the experiments, the deformed shape of the membrane was extracted from the DIC software with a 5 × 5 mm grid. The shape was then modelled in Abaqus 2018 (Dassault Systèmes) with shell elements and a finite-element simulation of such shape was performed adopting linear geometry, loaded with the pressure recorded in the experiment at the same time instant and a fictitious isotropic linear elastic material (which is proven not to affect the results of pressurised thin shells, see also [30]) with ETFE Poisson ratio $\nu = 0.43$ [5]. This method provided the complete stress field across the sample and was used to produce the experimental stress contour plots of Fig. 22(a). Moreover, this method was also used as validation of the isotropy assumption on a circular inflation test (strain rate 0.02%/s, 21 °C), see Fig. 20 and the contour plot for the same test in Fig. 21(a).

2.2. Test protocol

This section presents the experiments performed to characterise the thermomechanical response of ETFE membranes. They include (i) uniaxial relaxation on the DMA, (ii) uniaxial creep on the DMA, (iii) uniaxial cyclic loading on the electromechanical machine, (iv) biaxial inflation of circular foils, (v) biaxial inflation of elliptical foils, (vi) biaxial creep of pressurised circular foils, (vii) thermal expansion tests. A minimum of three specimens per condition were tested for each type of experiment. In addition to the tests reported below, the uniaxial tensile tests presented by Comitti and Bosi [5] will be employed to develop the constitutive model presented in the following sections.

Table 1
Short-term creep tests performed on DMA at different stress levels and temperatures for MD direction.

T [°C]	σ_{creep} [MPa]						
20	3	6	7.5	9	10.5	12	15
40	3	4.5	6	7.5	9		

2.2.1. Uniaxial relaxation tests

Relaxation tests were performed on the DMA at a constant strain of $\epsilon_{relax} = 1.5\%$, allowing the material to reach approximately 80% of the yield stress/strain after the loading ramp, before measuring its stress relaxation for four hours. This enabled to capture relaxation effects outside of the linear viscoelastic region. The strain level was achieved almost instantaneously, with a ramp of approximately 210 MPa/s, performed after a soaking phase of 10 min at the desired temperature. The procedure was repeated for samples aligned along both MD and TD directions for 0 °C, 25 °C, 40 °C, 50 °C and 60 °C. These tests were performed to assess the material relaxation when stretched to a certain position, analogous to the ETFE conditions when installed in single-tensioned foil envelopes.

2.2.2. Uniaxial creep tests

Creep tests were performed on the DMA at 20 °C and 40 °C, at different stress levels, for the MD direction only. The stress levels were achieved with the same loading ramp as the relaxation tests. The stress levels were selected aiming to describe the creep behaviour with an increasing creep stress that approached the yield stress, as detailed in Table 1. The creep time selected was variable, kept between 10 and 30 min, followed by a 90 min unloading phase. Such a short time interval was selected to prevent the onset of plasticity, which is likely to occur in a short timeframe if the creep stress is sufficiently close to the yield strength. In fact, preliminary 4-h creep and recovery tests were performed at 3 and 9 MPa at 23 °C, 40 °C and 60 °C, showing permanent strains in all the conditions excluding the case of 3 MPa at 20 °C.

These short-term creep tests were executed to observe the behaviour of ETFE foils under a persisting load, which is common in building applications, such as the pressure-induced creep of a cushion or the creep caused by snow load. For the latter example, a specific creep test set was executed on the DMA, along MD direction only, at T = 0 °C and σ_{creep} =9 MPa. Since this test was thought to simulate realistic load cases in cold environments, a loading ramp with a constant stress rate of 3.5 MPa/s (≈ 0.3%/s) was adopted.

2.2.3. Biaxial inflation tests

Biaxial tests were performed on the custom-made inflation setup, Fig. B.27, to characterise the material in a condition closer to applying the foil in tensile membrane structures. ETFE was inflated from circular and elliptical-shaped flat specimens to achieve principal stresses aligned with MD and TD's material directions at the deformed membrane's apex. The different shapes were selected to produce a different ratio between the principal stresses at that point of interest. For the circular membranes, the limited material orthotropy enabled the achievement of a nearly equibiaxial condition at the apex. The Von Mises stress and the equivalent strain $\bar{\epsilon} = \frac{1}{1+\nu}\sqrt{\frac{1}{2}\left[(\epsilon_1-\epsilon_2)^2+(\epsilon_1-\epsilon_3)^2+(\epsilon_3-\epsilon_2)^2+6\epsilon_6^2\right]}$ were utilised [8].

The inflation of circular foils was carried out at ambient temperature, 40 °C and 60 °C. At ambient temperature and 60 °C, three different constant pressure rate ramps were used to reproduce the strain rate range achieved in the uniaxial tensile tests, i.e. 10^{-2}%/s, 10^{-1}%/s and 1%/s. The same attempt was replicated when performing the elliptical-shaped inflation tests at ambient temperature. Furthermore, tests at 60 °C and 10^{-1}%/s strain rate were executed on elliptical specimens. The tests on elliptical membranes were performed by changing the material orientation and keeping the short axis aligned with either MD (labelled MD tests) or TD (labelled TD tests) directions. The ambient temperature for these tests was 23.5 °C with a standard deviation of 1.5 °C. It should be noted that the pressure rate measured in the tests was not proportional to the voltage input rate due to the changes in the volume of the inflated chamber and limitations on the flow rate of the equipment. As a result, the pressure rates achieved caused the measured strain rates to differ from the aimed values, particularly for the highest strain rate condition. Table 2 summarises the conditions investigated in the study.

Table 2
List of the biaxial inflation tests performed, reporting the average equivalent strain rate $\dot{\bar{\epsilon}}$ achieved at the apex of the inflated samples at the indicated pressure rate and average temperature. Tests not performed for specific conditions are labelled with –.

$\dot{p}$	T	$\dot{\bar{\epsilon}}$		
		Circular	Elliptical - MD	Elliptical - TD
[Pa/s]	[°C]	[%/s]		
300	25	0.02	0.02	0.02
	60	0.04	–	–
1200	22	0.06	0.05	0.06
	40	0.08	–	–
	60	0.1	0.1	0.1
2700	23.5	0.2	0.2	0.2
	60	0.14	–	–

2.2.4. Biaxial creep tests

An additional investigation on the biaxial behaviour involved a creep condition, achieved by performing 8-h inflation tests at a ≈10 MPa stress level on circular specimens, at T = 21 °C. As described before, under material isotropy assumption, the stress at the apex of the membrane was obtained through the expression $\sigma = \frac{pR}{2t}$. The approximately constant stress state over time was achieved by imposing a nonlinear time-dependent pressure input defined by inverting the above expression. In particular, using the ambient temperature results of a constant pressure rate test, it was possible to fit a polynomial function relating the strain and the radius of curvature R at the apex of the circular membrane as $R = f(\bar{\epsilon})$. The use of a preliminary version of the developed model allowed the simulation of a creep biaxial test, providing the biaxial strains $\bar{\epsilon}$. The pressure input required to achieve the target stress was then calculated as $p = \frac{2t\sigma}{R(\bar{\epsilon})}$ by imposing the desired stress and the radius R from the simulated strains at each time step of the simulation. The resulting pressure signal is provided in Fig. B.28. Due to material variability, the average initial stress levels achieved was σ_{max} = 9.76 MPa, which relaxed 8% over 4 h.

2.2.5. Uniaxial cyclic tests

Cyclic uniaxial tests were performed at −20 °C, 25 °C and 60 °C, for both MD and TD directions to understand the stiffness variation over cycles and the unloading path. The experiments were carried out on the universal testing machine described before, imposing a constant displacement rate of 5.5 mm/min (≈ $\dot{\epsilon}$ = 0.1%/s), both in the loading and unloading phases, for 10 cycles. Preliminary tests performed by the authors showed the absence of hysteresis at cyclic tests that reached approximately 50% of the yield point. Therefore, the strain amplitude of each cycle was approximately equal to $\epsilon_{cyc} = 1.5\%$, to reach stress levels close to the 80% of the yield point, as per uniaxial relaxation.

2.3. Thermal expansion tests

The thermal dilatation properties of the material were obtained by testing MD and TD rectangular laser-cut specimens of dimension 50 x 5 mm. The tests were performed using a Thermogravimetric Analyzer (TGA 5500, TA Instruments). The temperature was increased from −50 to 160 °C at a rate of 3 °C/min, after a soaking phase of 5 min at the

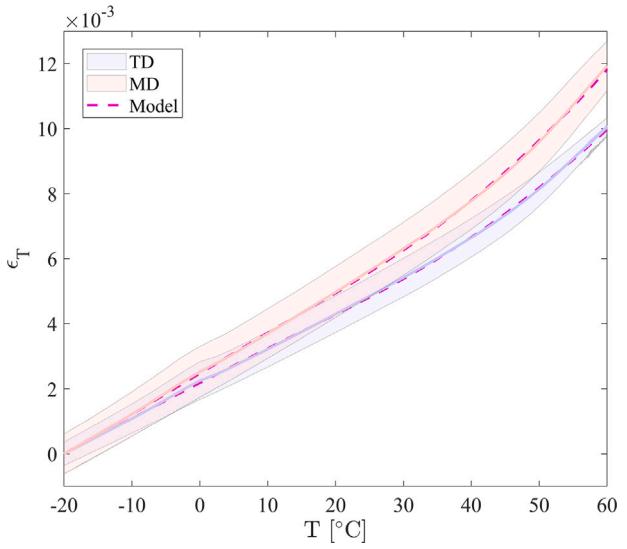

Fig. 2. Thermal dilatation of ETFE membranes along MD and TD, and fitting polynomial function used in the material model. Experimental average and standard deviation measures are reported with solid lines and areas, while the model is represented by a dashed line. (For interpretation of the references to colour in this figure legend, the reader is referred to the web version of this article.)

starting sub-ambient temperature. The results obtained, presented in Fig. 2, are similar in the two directions and approximate the results obtained recently in the literature [19]. It should be noted that an increase of ca. 15 °C produced thermal strains that are approximately 10% of the yield strain, which is relevant to the service state of the material. This thermal strain could modify the relaxation processes, especially for single-tensioned foils, which are stretched to fixed boundary positions and undergo relaxation. The evolution of the thermal strain with the temperature was fitted with a 6th order polynomial between the temperatures −20 °C and 60 °C. The polynomial functions $p(\mathrm{T})$, fitted on the strain-temperature data, were included in the implementation of the nonlinear model to determine the thermal strain as

$$\epsilon_T = p(\mathrm{T}_t) - p(\mathrm{T}_0), \tag{1}$$

where T is the temperature at the time instants t and $t = 0$. The coefficients determined for the polynomials are reported in Table A.6. The tests attempted in the out-of-plane direction gave inconsistent results because of the limited dimensions of the foil. Hence, given the minor influence of the out-of-plane direction in a membrane, the thermal expansion of the material in the through-thickness direction was considered a linear approximation of the average of the two main directions MD and TD.

3. Viscoelastic constitutive model and numerical implementation

The viscous features of ETFE need to be captured by a unified and comprehensive material model that can describe its temperature, time, and stress dependencies. The experimental campaign, whose results are reported in the following sections, showed a limited orthotropy of the material in the viscoelastic regime, although a more pronounced orthotropy develops in the viscoplastic regime, as shown in Fig. 1 . Therefore, we built two nonlinear viscoelastic models, one isotropic and the other orthotropic. The two models will be compared in Section 4. However, it is anticipated that the former model could be used for ETFE foils that can be approximated as isotropic materials, while the latter is helpful for viscoelastoplastic modelling or when specific foils and/or design criteria require differentiation of the response in the MD or TD directions. The linear viscoelastic models are presented first, before the nonlinear features are added.

3.1. Linear viscoelasticity

A linear viscoelastic constitutive law featuring a Generalised Kelvin element in the framework of the Boltzmann superposition principle has been adopted, such that

$$\boldsymbol{\epsilon} = \int_0^t \boldsymbol{D}(t-s)\frac{\partial \boldsymbol{\sigma}}{\partial s}\,ds. \tag{2}$$

Each term of the compliance matrix $\boldsymbol{D}$ is expressed through a Prony series representation as [31,32]

$$D_{jk} = D_{jk,0} + \sum_{i=1}^{N} D_{jk,i}\left(1 - e^{-\frac{t-s}{\tau_i}}\right), \tag{3}$$

and $D_{jk,0}$ is the instantaneous compliance of the Generalised Kelvin element corresponding to the single spring added in series to the N Kelvin elements, each characterised by the compliance $D_{jk,i}$ and relaxation time τ_i. In linear viscoelasticity, a common strategy adopted to include the temperature effects on the material behaviour is the time–temperature superposition principle (TTSP) to build creep compliance master curves from creep tests performed at different temperatures. Temperature variations are seen as analogous to strain rate or time variations, allowing for widening the time scale of the predictions compared to the laboratory time of the tests by shifting the temperature-dependent creep compliances in the time domain. Hence, the creep compliance master curves were obtained from four-hour creep tests at 1.5 MPa during a previous experimental campaign aimed at defining the linear viscoelastic domain and linear response [5]. The creep tests were executed at temperatures ranging from −20 °C to 65 °C along MD, TD and ID. The latter represents a direction at 45° to MD, used to characterise the in-plane shear behaviour by rotating the stress and strain tensors from the uniaxial loading direction to the material principal axes [5,33], avoiding wrinkling phenomena occurring in pure or simple shear tests [34]. The direction-dependent creep compliance master curves were created at the reference temperature $\mathrm{T_{ref}}$ = 20 °C by horizontally shifting all other temperature-dependent creep compliance curves (left shift if $\mathrm{T}<\mathrm{T_{ref}}$ and right shift if $\mathrm{T}>\mathrm{T_{ref}}$) through the shift factor $a_T = t/t'$, with t' being the reduce time scale. The temperature-dependent shift factor can be defined through the Arrhenius law

$$\log_{10} a_T = \log_{10}\frac{\tau(\mathrm{T})}{\tau(\mathrm{T_{ref}})} = -\frac{E_a}{2.303R}\left(\frac{1}{\mathrm{T}} - \frac{1}{\mathrm{T_{ref}}}\right), \tag{4}$$

where E_a is the activation energy and R is the universal gas constant. The creep compliance master curve for the isotropic model, obtained by averaging the MD, TD and ID creep tests, is reported in Fig. 3, while the analogue curves obtained in [5] for each orientation are reported in the Appendix A.

All the experimental master curves were separately fitted with a Prony series of twenty-two compliance parameters $D_{jk,i}$, having defined twenty-one relaxation times τ_i evenly spaced in a logarithmic scale between 10^{-12} and 10^{11}. To reach shorter time scales compared to the measured data, the tail of the master curve (shifted compliance values of the tests below 15 °C) was extrapolated with a linear fit in the logarithmic time-strain domain of Fig. 3, until a time of 10^{-12} s. These data were included in the master curve fitting process to avoid ill-conditioned predictions at lower temperatures and high strain rates.

The fitted master curves of the isotropic model, D_{ISO} and the shear compliance obtained through Hooke's law, $D_{\mathrm{ISO\text{-}ID}} = D_{\mathrm{ISO}}(1+\nu)$, and those of the orthotropic model, D_{MD}, D_{TD} and D_{ID}, are compared in Fig. 4. The compliances in directions MD and TD are comparable with the results obtained by the averaged compliance D_{ISO}. The difference that exists between D_{ID} and $D_{\mathrm{ISO\text{-}ID}}$ at higher temperatures and longer times produces a softer response with a shape of the master curve that mimics the ones of MD and TD directions.

The fitted master curves, whose parameters are reported in Table A.5, were used to form orthotropic and isotropic plane stress

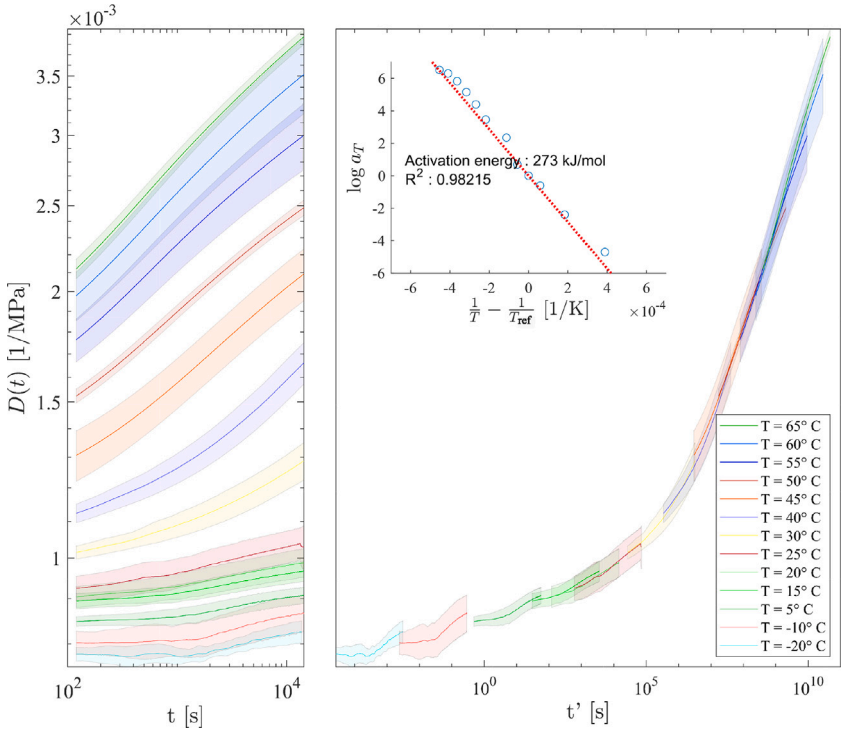

Fig. 3. Left: Average engineering creep compliance $D(t)$ from creep test performed at 1.5 MPa along MD, TD and ID for different temperatures in the range −20 °C to 65 °C. Right: Engineering creep compliance master curve at T_{ref} = 20 °C, obtained by horizontally shifting the compliance curves at other temperatures through the time shift factor a_T. The inset shows the experimental time shift factors and their fitting through the Arrhenius law, Eq. (4). (For interpretation of the references to colour in this figure legend, the reader is referred to the web version of this article.)

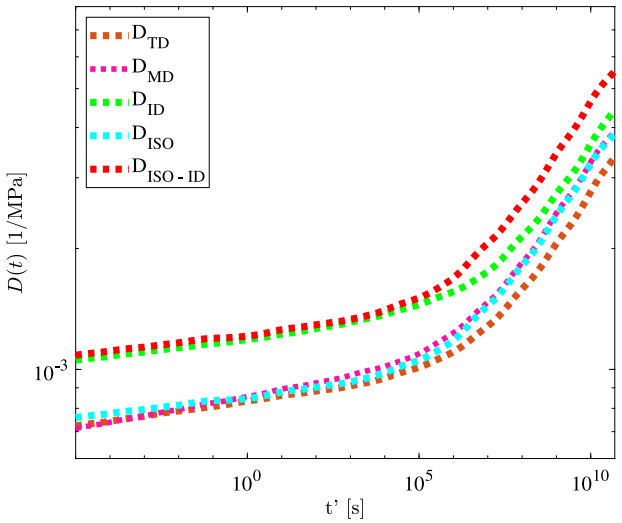

Fig. 4. Creep compliance master curves of the isotropic (D_{ISO} and $D_{ISO\text{-}ID}$) and orthotropic (D_{MD}, D_{TD} and D_{ID}) models as a function of the reduced time t'. (For interpretation of the references to colour in this figure legend, the reader is referred to the web version of this article.)

models. Assigning to each direction a number, 1≡MD, 2≡TD, 6≡ID, the orthotropic model was built from (2) with a compliance matrix

$$D = \begin{bmatrix} D_{11} & D_{12} & 0 \\ D_{21} & D_{22} & 0 \\ 0 & 0 & D_{66} \end{bmatrix}, \tag{5}$$

where the general expression for strains in reduced time t' is

$$\epsilon_j(t') = \int_0^{t'} \left[D_{jk,0} + \sum_{i=1}^{N} D_{jk,i} \left(1 - e^{-\frac{t'-s}{\tau_i(T_{ref})}} \right) \right] \frac{d\sigma_k}{ds} ds, \tag{6}$$

with $j,k = \{1,2,6\}$. Further assumptions were made to complete the model, such as $D_{12} = D_{21} = \nu \dfrac{(D_{11} + D_{22})}{2}$, where $\nu = 0.43$ is the Poisson's ratio determined from digital image correlation measurements of the transverse strain during uniaxial tensile tests [5]. Moreover, suppose an estimation of the out-of-plane (i.e. through-thickness) engineering strain ϵ_3 is needed. In that case, in the absence of direct measurements, it can be obtained as $\epsilon_3 = D_{13}\,\sigma_1 + D_{23}\,\sigma_2$, where D_{13} and D_{23} can be assumed equal to D_{12}. In the isotropic model, the additional equivalences $D_{11} = D_{22}$ and $D_{66} = D_{11}\,(1+\nu)$ are set.

3.2. Nonlinear viscoelasticity

Several ways of including nonlinearities in a viscoelastic constitutive law exist in the literature, and a particularly effective one, thanks to its simplicity and analogy to the Boltzmann superposition principle, is the single integral representation proposed by Schapery for a Generalised Kelvin element [35]:

$$\epsilon_j(t', T, \sigma) = \int_0^{t'} \left[g_0 D_{jk,0} + \sum_{i=1}^{N} g_1 D_{jk,i} \left(1 - e^{-\frac{t-s}{\tau_i a_T a_\sigma}} \right) \right] \frac{d(g_2\sigma_k)}{ds} ds, \tag{7}$$

where the four functions a_σ, g_0, g_1, g_2 incorporate nonlinearities to the linear Boltzmann integral. It has been shown that, for many materials [35,36], high accuracy in the modelling can be achieved only by considering a_σ, thus imposing $g_0 = g_1 = g_2 = 1$. The stress shift factor a_σ modifies the internal time of the material analogously to the effect of temperature [31,37], transforming the linear dashpots of the Generalised Kelvin element into non-Newtonian liquids. Among the different contributions in the literature, a common approach is to consider the Eyring equation of reaction rates [38] to calculate a_σ as [39–42]

$$a_\sigma = \frac{\sigma_{ey}}{\sigma_0 \sinh\left(\frac{\sigma_{ey}}{\sigma_0}\right)}, \tag{8}$$

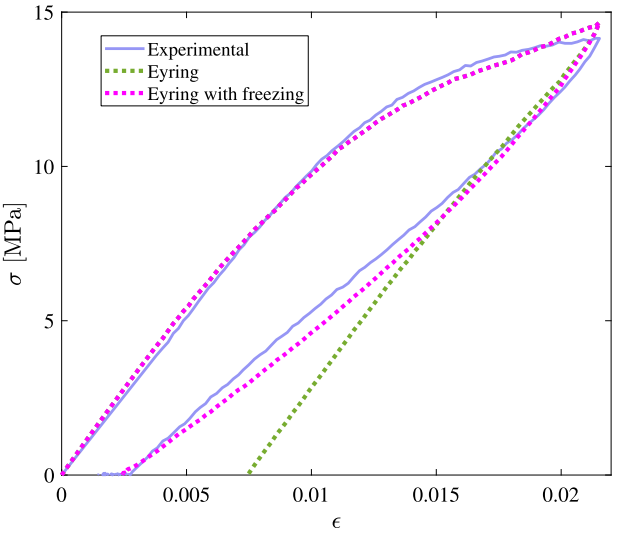

Fig. 5. Comparison of the response of the nonlinear viscoelastic model with and without freezing the Eyring shift factor a_σ at the peak of a load–unload uniaxial tensile test at 23 °C along MD. (For interpretation of the references to colour in this figure legend, the reader is referred to the web version of this article.)

where $\sigma_0 = \dfrac{RT_0}{V}$, σ_{ey} is the effective stress, often assumed as the equivalent Von Mises stress $\bar{\sigma}$ (see also Eq. (21)), and V is material the activation volume. The Eyring model was selected since ETFE is commonly used in building applications under its glass transition temperature, assuming the other Schapery's functions $g_0 = g_1 = g_2 = 1$. Other nonlinear viscoelastic models based on Schapery's equation, such as the Free Volume model [37], are less suitable to model a polymer in the glass or glass-forming region. However, Xia et al. [43] highlighted how an Eyring stress shift factor model, alongside other widely spread nonlinear viscoelastic descriptions, is unable to predict the curvature change in a stress–strain plot during the unloading phase. This effect, also found consistently in the present work on ETFE, can be overcome by freezing the shift factor during each unloading step, keeping a_σ at the last value achieved on the preceding loading path. This strategy was incorporated into the constitutive law for ETFE, as shown in the following section on the numerical implementation. The difference between using the classic Eyring theory and the one which includes the shift factor freezing can be observed in Fig. 5 for a representative ETFE uniaxial loading-unloading test carried out at ambient temperature along MD.

It should be noted that the constitutive models presented above are referred to the mechanical strains ϵ only. To provide a complete framework for the strain ETFE undergoes, the thermal components of the total strain tensor are also included in the model as $\epsilon_{\text{total}} = \epsilon + \epsilon_T$, where ϵ_T is defined in Eq. (1).

3.3. Numerical implementation of the constitutive law

The models presented above were implemented in a MATLAB code and an ABAQUS User Material Subroutine (UMAT) through a recursive algorithm necessary to solve the time integrals and to limit the storage of the contributions to the final strains across the whole load time history [5,33,44]. Eq. (7), written in the following as one-dimensional to simplify the notation, can be expressed as

$$\epsilon(t') = \int_0^{t'} \left[D_0 + \sum_{i=1}^{N} D_i \left(1 - e^{-\frac{t'-s}{\tau_i}}\right) \right] \frac{d\sigma}{ds} ds. \tag{9}$$

Assuming the material stress is null at the beginning of the simulation, the integration of Eq. (9) gives

$$\epsilon = \left(D_0 + \sum_{i=1}^{N} D_i \right) \sigma^{t'} - \sum_{i=1}^{N} D_i \int_0^{t'} \left(1 - e^{-\frac{t'-s}{\tau_i}}\right) \frac{d\sigma}{ds} ds, \tag{10}$$

where the time-dependent component of the strain can be isolated and termed hereditary integral, $q^{t'}$. Defining the time increment as Δt, or $\Delta t'$ when referring to the reduced time, $q^{t'}$ can be split into two parts as

$$\epsilon = \left(D_0 + \sum_{i=1}^{N} D_i \right) \sigma^{t'} - \sum_{i=1}^{N} D_i \left[\int_0^{t'-\Delta t'} \left(1 - e^{-\frac{t'-s}{\tau_i}}\right) \frac{d\sigma}{ds} ds + \int_{t'-\Delta t'}^{t'} \left(1 - e^{-\frac{t'-s}{\tau_i}}\right) \frac{d\sigma}{ds} ds \right], \tag{11}$$

thus separating the hereditary contributions from the one of the current increment, from $t' - \Delta t'$ to t'. The integral spanning from 0 to $t' - \Delta t'$ can be written as

$$\int_0^{t'-\Delta t'} \left(1 - e^{-\frac{t'-s}{\tau_i}}\right) \frac{d\sigma}{ds} ds = \int_0^{t'-\Delta t'} \left(1 - e^{-\frac{t'-\Delta t'+\Delta t'-s}{\tau_i}}\right) \frac{d\sigma}{ds} ds = e^{-\frac{\Delta t'}{\tau_i}} \int_0^{t'-\Delta t'} \left(1 - e^{-\frac{t'-\Delta t'-s}{\tau_i}}\right) \frac{d\sigma}{ds} ds, \tag{12}$$

to produce a resulting integral which is similar to $q^{t'}$ of Eq. (10), but referred to the time history before the current step and defined as $q^{t'-\Delta t'}$. Consequently, Eq. (11) can be written as

$$\epsilon = \left(D_0 + \sum_{i=1}^{N} D_i \right) \sigma^{t'} - \sum_{i=1}^{N} D_i \left[e^{-\frac{\Delta t'}{\tau_i}} q^{t'-\Delta t'} + \int_{t'-\Delta t'}^{t'} \left(1 - e^{-\frac{t'-s}{\tau_i}}\right) \frac{d\sigma}{ds} ds \right]. \tag{13}$$

If the stress is assumed to be linear across the increment, it is possible to express the former equation as

$$\epsilon = \left(D_0 + \sum_{i=1}^{N} D_i \right) \sigma^{t'} - \sum_{i=1}^{N} D_i \left[e^{-\frac{\Delta t'}{\tau_i}} q^{t'-\Delta t'} + \tau_i \frac{\sigma^{t'} - \sigma^{t'-\Delta t'}}{\Delta t'} \left(1 - e^{-\frac{\Delta t'}{\tau_i}}\right) \right], \tag{14}$$

which gives accurate results if the time increment $\Delta t'$ is appropriate and sufficiently small. In particular, it is advised to refine the time step whenever the material changes the loading history. If the common terms of Eq. (14) are grouped, the mechanical strain can be expressed as

$$\epsilon = \left\{ D_0 + \sum_{i=1}^{N} D_i \left[1 - \frac{\tau_i}{\Delta t'} \left(1 - e^{-\frac{\Delta t'}{\tau_i}}\right) \right] \right\} \sigma^{t'} - \sum_{i=1}^{N} D_i \left[e^{-\frac{\Delta t'}{\tau_i}} q^{t'-\Delta t'} - \tau_i \frac{\sigma^{t'-\Delta t'}}{\Delta t'} \left(1 - e^{-\frac{\Delta t'}{\tau_i}}\right) \right]. \tag{15}$$

By defining

$$g_i = \tau_i \frac{\left(1 - e^{\frac{-\Delta t'}{\tau_i}}\right)}{\Delta t'}, \tag{16}$$

$$\tilde{D}^{t'} = \left(D_0 + \sum_{i=1}^{N} D_i \left(1 - g_i\right) \right), \tag{17}$$

$$F^{t'-\Delta t'} = \sum_{i=1}^{N} D_i \left(e^{-\frac{\Delta t'}{\tau_i}} \; q_i^{t'-\Delta t'} - g_i \; \sigma^{t'-\Delta t'} \right), \tag{18}$$

and generalising the expression in Eq. (14) for every component $j, k \in [1, 2, 6]$, Eq. (15) can be written as

$$\epsilon_j(t') = \tilde{D}_{jk}^{t'} \; \sigma_k^{t'} - F_j^{t'-\Delta t'}. \tag{19}$$

The numerical implementation above can be found in a MATLAB code at github.com/fbosi/ETFE-NLVE-model, for the calculation of the strain tensor of a single plane stress element. The quantities that have to be provided as inputs are a time array, the temperature values and stress tensor $\boldsymbol{\sigma} = [\sigma_1, \sigma_2, \sigma_6]^{\mathrm{T}}$ associated with each time instant. However, the use of finite elements (FE) analyses is required for more

complex geometries. Therefore, the formulation above was reversed to predict the stresses from the strain history as

$$\sigma_j(t') = \Lambda^{t'}_{jk}\left(\epsilon^{t'}_k + F^{t'-\Delta t'}_k\right), \tag{20}$$

where $\Lambda^{t'}$ is the inverse of the time-dependent compliance matrix $D^{t'}$. This formulation was then implemented both in the MATLAB code and in an Abaqus User Material Subroutine (UMAT) present at the same link above. All the formulations include the freezing of the stress shift factor. The freezing of the stress shift factor was implemented differently from the indications of Xia et al. [43], which use the equivalent Von Mises stress rate $\dot{\bar{\sigma}}$ to identify whether the material is in an unloading phase. To separate the stress relaxation load case from the unloading behaviour, we introduced a condition on the rate of the maximum in-plane strain $\dot{\epsilon}_{\max} = \dfrac{\partial(\max(\epsilon_j))}{\partial t}$, with $j = \{1, 2, 6\}$. The effective stress σ_{ey} used in the Eyring model for the current time step can be accordingly expressed as

$$\sigma^t_{ey} = \begin{cases} \bar{\sigma}^t & \text{if } \dot{\epsilon}_{\max} \geq 0 \\ \bar{\sigma}^{t-\Delta t} & \text{otherwise.} \end{cases} \tag{21}$$

Using this expression had positive outcomes when predicting both unloading and stress relaxation cases, and was therefore adopted throughout the validation performed in Section 4. As stated earlier, engineering quantities were considered in the model formulation because of the low yield strain limit of ETFE. However, FE packages work with finite strain descriptions when dealing with nonlinear analyses and membrane elements. In the Abaqus UMAT, the engineering strains need to be retrieved from the input variables. In particular, the left Cauchy–Green tensor C was computed from the deformation gradient F as $C = F^T F$. Through the polar decomposition of the deformation gradient $F = RU$ in rotation and stretch tensor, it is possible to express the stretch as $U = C^{1/2}$ and consequently the engineering strain tensor as $E = U - I$, I being the identity matrix. After the calculation of the engineering stress σ_{PK1} (1st Piola–Kirchhoff stress) through the recursive algorithm, the Cauchy stress tensor is calculated and assigned to Abaqus `sigma` quantity as

$$\sigma_{\text{Cauchy}} = \frac{\sigma_{\text{PK1}} F^T}{J}, \tag{22}$$

with $J = \det(F)$. The implementation of the constitutive law allowed us to perform simulations of every experimental condition and was extensively used in the process of fitting the material parameters and validating them on independently acquired data.

3.4. Nonlinear viscoelastic model fitting

The determination of the material parameter of the nonlinear constitutive models, i.e. the Eyring activation volume V, was performed using a fitting process that employed the numerically implemented constitutive law of Section 3.3. For each model considered, namely isotropic and orthotropic, Table 3 reports the experiments carried out, distinguishing whether the test was used for the nonlinear model fitting or its validation on independent data not used in the fitting procedure. To avoid using data which included plasticity, a threshold was placed on the limit strain of the data utilised for the fitting procedure, equal to an equivalent strain of $\bar{\epsilon} = 2.5\%$. Moreover, the short-term creep tests were not used as some presented residual strains after the unloading phase, meaning plasticity had occurred. The tests used in fitting the orthotropic material model were the uniaxial relaxation tests and the equibiaxial tests at a constant pressure rate. In this way, the final nonlinear model could be fitted on loading conditions other than creep, already used in the linear viscoelastic modelling. For the isotropic model, using the same tests provided inaccurate predictions in the validation process of the creep tests. A transition that happens during the relaxation process, discussed in Section 4.3, was triggering higher nonlinear parameters, which were causing the creep strain rate prediction to be higher than the experimental one. Therefore, only the equibiaxial experiments were adopted for the fitting of the isotropic model.

Table 3
List of experiments performed and their use in the nonlinear viscoelastic modelling of ETFE.

Test executed	Orthotropic model	Isotropic model
Uniaxial tensile relaxation Uniaxial tensile creep	Fitting Validation	Validation
Biaxial inflation of circular membranes	Fitting	
Biaxial inflation of elliptical membranes Biaxial creep of circular pressurised membranes Uniaxial tensile cyclic tests Uniaxial tensile tests at constant strain rates [5]	Validation	
Thermal expansion test	Fitting	

The results of the model predictions were used to build an error measure that was minimised as a function of the unknown material parameter V. The error function was built considering the normalised difference between the area under the experimental curve A_{exp} and the one under the predicted curve from the developed constitutive model A_{model} as

$$\text{Error} = \sum_{m=1}^{K}\left|\frac{A_{\text{model,m}} - A_{\text{exp,m}}}{A_{\text{exp,m}}}\right|, \tag{23}$$

where K is the total number of each type of experiment m. Each area is obtained by computing the incremental area at every instant n of the test until the last step N considered, with a trapezoidal approximation as

$$A = \sum_{n=2}^{N}(x^n - x^{n-1})\frac{1}{2}(\bar{\sigma}^n + \bar{\sigma}^{n-1}). \tag{24}$$

The quantity x considered was different depending on the test procedure. In constant strain rate tests, or constant pressure rate inflation experiments, $x = \bar{\epsilon}$, the equivalent strain. For relaxation or creep tests, the area was computed using x = time. This significantly reduced the loading ramp's influence on the error measure. In this study, `fmincon` (Interior Point Algorithm) algorithm of MATLAB was used to minimise the error between the experiments and model predictions. The error measure was also used in the validation of the material models, also including the R^2 value of the model or the deviation in particular points, as it will be shown in the next section.

The results of the fitting process provided activation volumes $V_{\text{ortho}} = 2.74 \cdot 10^{-6}$ m^3/mol and $V_{\text{iso}} = 2.52 \cdot 10^{-6}$ m^3/mol, for the orthotropic and isotropic models, respectively.

4. Results and model validation

The isotropic and orthotropic constitutive models developed and numerically implemented in the previous section were validated by comparing the experimental results with the prediction from FE simulations, whose models were created according to the experimental setups, reproducing the same loading and boundary conditions. These models included (i) uniaxial dumbbell specimens, (ii) uniaxial rectangular samples for DMA, (iii) biaxial circular and elliptical inflation specimens. The elements used in the FE simulations were 3D membrane linear elements (Abaqus M3D6 elements), and the analyses accounted for nonlinear geometric effects. The temperature and the loading conditions were extracted from the experimental data and given as input to Abaqus as pre-defined fields, i.e. pressure loading and displacement loading with custom amplitudes.

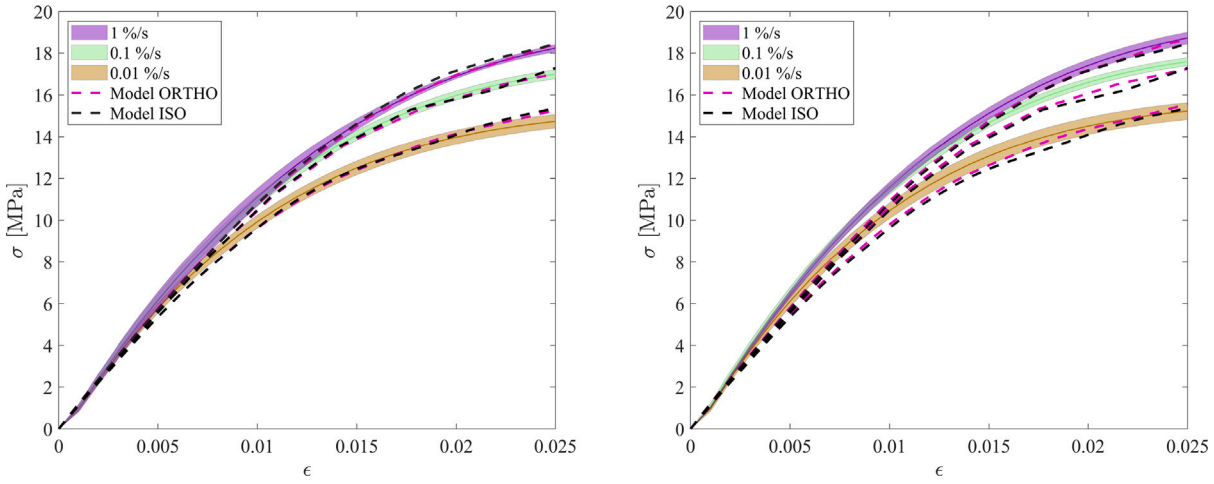

Fig. 6. Strain rate effects on ETFE engineering stress–strain curve at T_{amb} = 23 °C along MD (left) and TD (right). The solid line represents the average experimental value, while the coloured area is the standard deviation [5]. The dashed lines represent the FE simulations of a dumbbell specimen with isotropic (black) and orthotropic (pink) models. (For interpretation of the references to colour in this figure legend, the reader is referred to the web version of this article.)

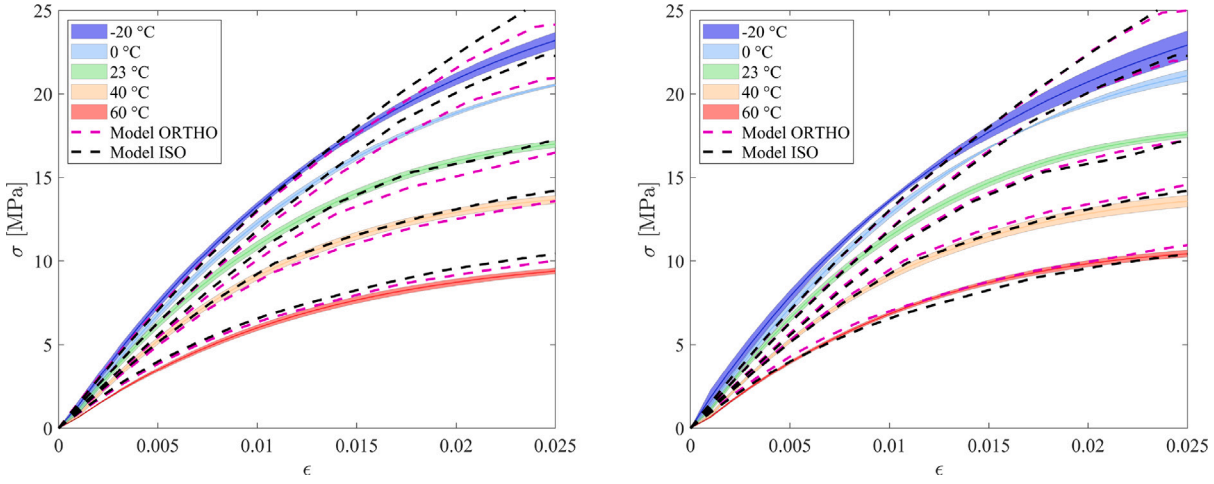

Fig. 7. Temperature effects on ETFE engineering stress–strain curves at 0.1%/s strain rate along MD (left) and TD (right). The solid line represents the experimental average value, while the coloured area is the standard deviation [5]. The dashed lines represent the FE simulations of a dumbbell specimen with isotropic (black) and orthotropic (pink) models. (For interpretation of the references to colour in this figure legend, the reader is referred to the web version of this article.)

4.1. Uniaxial tensile tests

The first set of tests presented are the uniaxial tensile experiments at constant strain rate tests performed at different strain rates and isothermal conditions, shown in Figs. 6 and 7, respectively, for MD (left) and TD (right) directions. The agreement between the models and the experimental data is excellent (min R^2 = 0.9837), capturing correctly the nonlinear viscoelastic effects at different strain rates and temperatures. Similar outcomes were obtained for ID, the direction at 45° to MD and TD, used to characterise the in-plane shear behaviour by rotating the stress and strain tensors from the uniaxial loading direction to the material principal axes [5,33]. These plots are shown in Appendix C.1.

The highest discrepancy was found at sub-ambient temperature, −20 °C, with an error of 12% (MD) and 14% (TD) of the stress prediction at ϵ = 2.5% for the isotropic model, while the orthotropic performed better, with 4.5%(MD) and 10% (TD) of maximum deviation. The tests along ID direction have discrepancies of the same range, with a maximum of 10.9% for the isotropic model at −20 °C, and 12.6% for the orthotropic at 60 °C, as shown in Fig. C.29. The different behaviour of the shear master curve for the two models, as per Fig. 4, resulted in the isotropic model being more accurate at higher temperatures, whilst the orthotropic was more effective at sub-ambient thermal conditions.

4.2. Uniaxial tensile cyclic tests

The cyclic test results are shown in Fig. 8 for MD (left) and TD (right) directions, respectively. Since the tests were displacement-driven but dumbbell specimens were adopted, it was not possible to achieve the same strain value for all the specimens. Therefore, it was impossible to perform meaningful average curves and only the results of one sample are shown; however, good repeatability was obtained for the other samples tested. Additionally, only two cycles (over a total of ten) were reported to help the visualisation of the curves. It can be seen that the material models follow the uniaxial response during the loading phase less accurately than described in Section 4.1, showing an average discrepancy between experiments and simulations of 2.5%. The freezing of the shift factor allows a smooth switch between the loading and unloading conditions, maintaining a similar initial stiffness in all the loading phases over the cycles, as found experimentally and consistently with other findings in the literature [45,46]. However, the simulated unloading phase shows discrepancies with data, providing more hysteresis in the stress–strain plots. The hysteresis area

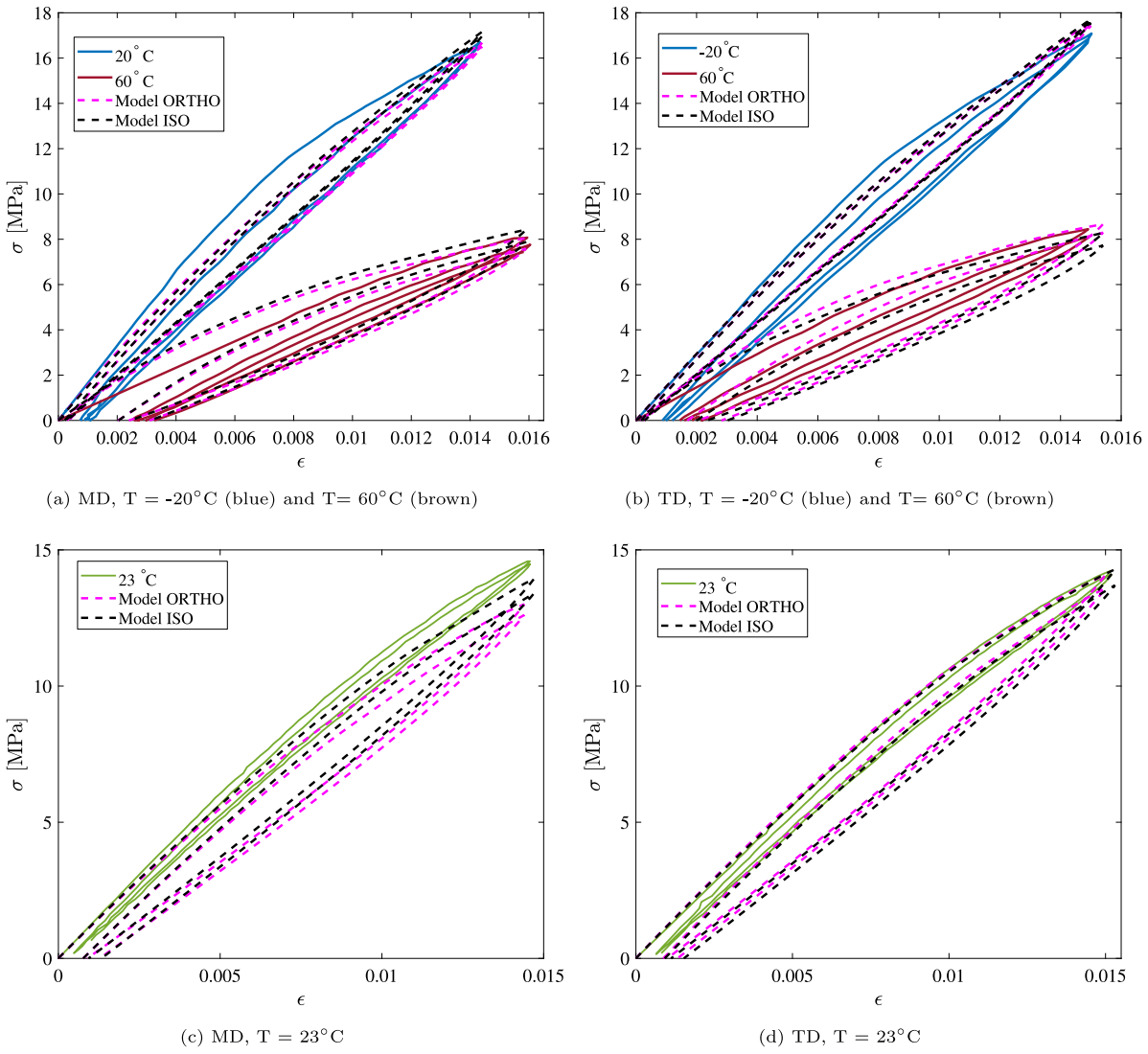

Fig. 8. ETFE engineering stress–strain curve for uniaxial tensile cyclic tests, where only two cycles are shown for visual clarity. The solid line represents the experimental value, while the dashed lines represent the FE simulations with a dumbbell specimen of the orthotropic (pink) and isotropic (black) models. (For interpretation of the references to colour in this figure legend, the reader is referred to the web version of this article.)

accumulated for ten cycles in the experimental procedure is between 50 and 70% inferior to the one predicted with the models, with the most divergent response being at ambient temperature when using the orthotropic model, as per Fig. 8(c). The higher hysteresis predicted by the model with respect to a low experimental hysteresis area of ETFE can be caused by the rigidity of the model due to the freezing of the stress shift factor, which drives the unloading path depending on the value of the last stress achieved in the loading phase. Despite producing higher hysteresis, the freezing behaviour was found to be the more accurate strategy available to capture the unloading behaviour, as the use of the sole Eyring theory (or other stress shift-factor-based laws [43]) produced a more inaccurate response, see also Fig. 5. An alternative fitting of the stress shift factor law, according to strain rate, temperature, and stress level of the cyclic tests, could have been performed, although many tests should have been added to the experimental campaign. Considering the reduced material hysteresis in the viscoelastic phase and the limited design use of ETFE dissipated energy in membrane structures, the shift factor freezing strategy was assumed to be adequate to model the polymer's behaviour.

4.3. Uniaxial relaxation tests on DMA

Relaxation tests are presented in Fig. 9 in a logarithmic time scale, which allows to observe more closely the complete stress relaxation process. The loading ramp of these tests was rapid (>15%/s), aiming to achieve "instantaneously" the desired conditions. This often caused an overshooting of the strain in the equipment, which could not stop promptly at the desired strain and slightly surpassed it. Such a fast ramp of 0.1 s also produced an overshoot of stress in the model predictions of the loading ramp, as both isotropic and orthotropic constitutive relations are less accurate beyond the maximum strain rate of 1%/s used in the characterisation. Considering that, for the sake of the model validation, it is more relevant to observe the behaviour during the relaxation process rather than during the high-speed loading ramp. Hence, scaling of the initial experimental loading ramp input for the FE model was made to guarantee a similar stress starting point of the relaxation process with the experimental data. The average corrections applied at the different stress levels, which correspond to the overshooting, amount to ≈12% of the maximum value.

It is possible to notice how the two models performed quite similarly to each other, only diverging in the tests at 0 °C along MD, where the

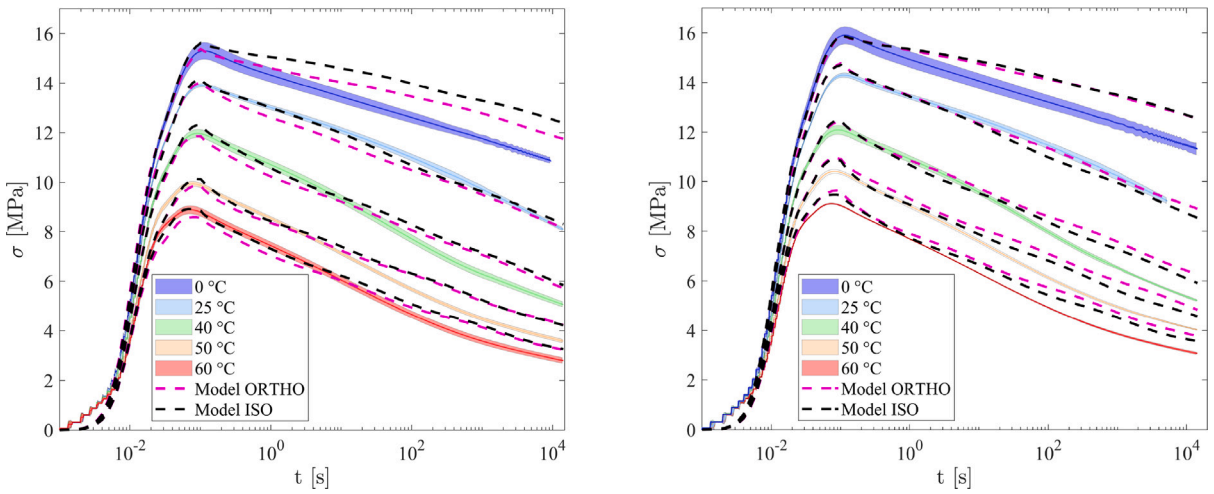

Fig. 9. Uniaxial relaxation tests at different temperatures at ϵ_{relax} = 1.5% along MD (left) and TD (right). The solid line represents the average value, while the coloured area is the standard deviation. The dashed lines represent the FE simulations of a rectangular specimen obtained with the orthotropic (pink) and isotropic (black) models. (For interpretation of the references to colour in this figure legend, the reader is referred to the web version of this article.)

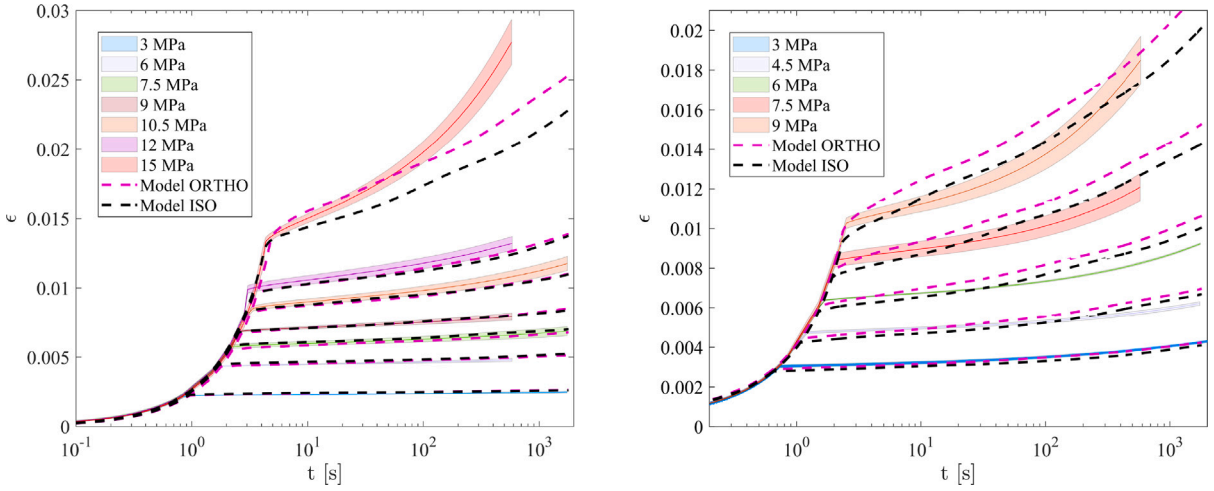

Fig. 10. ETFE engineering strain-time creep tests curves at T = 20 °C (left) and T = 40 °C (right) along MD, at different stress levels. The solid line represents the experimental average value, while the coloured area is the standard deviation. The dashed lines represent the FE simulations of a DMA rectangular specimen with the orthotropic (pink) and isotropic (black) models. (For interpretation of the references to colour in this figure legend, the reader is referred to the web version of this article.)

isotropic model response is stiffer (15.5% more rigid than the experiment compared to +9.5% of the orthotropic model). The predictions are generally accurate, with a maximum percentage deviation for the orthotropic model of 23% for the tests along the TD direction at 60 °C, which amounts to only 0.7 MPa. The material response approximately resembles a linear behaviour in the log scale during the initial phases of the relaxation step of Fig. 9, corresponding to an exponential decay of the stress. The slope of the predicted curve diverges from the experimental data after approximately 100 s, especially for the tests at temperatures higher than 25 °C. The use of relaxation tests in fitting the stress shift factor in the orthotropic model did not improve this behaviour, attributed to the presence of a secondary transition in the time–temperature domain, happening at ca. 40 °C [5]. Although some attempts exist [47] to create more complex shift laws to account for these effects, such transitions cannot be predicted accurately with the current temperature shift factor equations. Nevertheless, given the relatively small error observed, the model is considered sufficiently accurate.

4.4. Uniaxial creep tests on DMA

The results of the creep tests are presented in Fig. 10 in a logarithmic time scale, which allows to observe more closely the complete creep strain process. As for the relaxation tests, the loading ramp's high speed caused an overshoot of the stress achieved in both experiments and models. Similar readjustments to what was mentioned in Section 4.3 were necessary in the FE simulations input to obtain a similar strain value between the models and the experimental data after the fast loading ramp, and hence a fair comparison between the numerical predictions and measurements under creep. The correction factors used for the loading ramp were, on average, 0.87 and 0.83 for the isotropic and orthotropic models, respectively. These corrections testify the average differences of 13% and 17% between the models' predictions and experiments for very high strain rates (18%/s on average, with peaks of 50%/s), well outside the ranges of characterisation of the models.

It is noticeable in all curves that the orthotropic model is less stiff than the isotropic one, thus resulting in higher creep strains and strain rates during creep tests. At 20 °C, the isotropic model predictions have an average error (in the strain-time plot) of 4.5% for all the stress levels up to 12 MPa, while the orthotropic model reaches an average

Table 4
Average residual strains after 90 min of recovery time at the end of short-term creep tests executed on the DMA setup at different stress levels and temperatures for ETFE samples along MD direction. In red are the values that exceed the threshold of 0.05% [48].

σ_{creep} [MPa]	T [°C]	$\epsilon_{residual}$ %
3		0.007 ± 0.005
6		0.016 ± 0.007
7.5		0.023[a]
9	20	0.049[a]
10.5		0.089 ± 0.017[a]
12		0.182 ± 0.017[a]
15		0.329 ± 0.02[a]
3		–[b]
4.5		0.05 ± 0.002
6	40	0.101 ± 0.002
7.5		0.112 ± 0.011
9		0.223 ± 0.048[a]

[a] Strain recovery performed on less than three tests. The values without an error range represent a single recovery test.
[b] No strain recovery executed.

discrepancy of 23%. The model's accuracy at ambient temperature, up to the creep stress of 12 MPa is very good. At 40 °C, an average error of 23% and 21% are found in the predictions of the isotropic and orthotropic models, respectively, up to 7.5 MPa. In this case, it can be observed how the experimental and simulation curves show some differences, especially towards the end of the test. The same discrepancy, although more evident, exists for the stress levels of 15 MPa at 20 °C and 9 MPa at 40 °C, which showed a diverging slope of the curves starting a few seconds after the beginning of the creep phase, where the experimental response exhibited a higher strain rate. At the end of the tests, the strain rate differences between tests and the isotropic and orthotropic constitutive laws were respectively 72% and 68% for the test at 15 MPa, 20 °C, and 47% and 29% for the test at 9 MPa, 40 °C. These discrepancies between the model predictions and measurements are caused by the development of plasticity, not captured by the current nonlinear viscoelastic models. This was confirmed by measuring the permanent strains after unloading and strain recovery of the specimens. Table 4 displays all the tests performed with the average residual strain $\epsilon_{residual}$ after 90 min of strain recovery, where in red are the values that surpassed the 0.05% limit employed to distinguish whether viscoplasticity had occurred [48]. The quantities reported are noticeably small; however, the DMA has a displacement accuracy of 5 nm, corresponding to an engineering strain accuracy of $\approx 3 \cdot 10^{-5}$%, so that the measure of the residual strain reported in Table 4 can be considered reliable. The viscoelastic strain recovery could be a long process; however, the average and minimum strain rates at the end of the tests were $-1.42 \cdot 10^{-}6$%/s and $-1.31 \cdot 10^{-}5$%/s (for the test at 9 MPa at 40 °C), respectively. These rates are very small and would further reduce; hence, 90 min of unloading were considered sufficient for such short-term creep tests. According to the criterion of Suleman [48], plasticity onsets at stresses higher than 9 MPa at 20 °C and 4.5 MPa at 40 °C in this creep tests campaign. Another cause for the discrepancies observed, especially at 40 °C, can be due to the secondary transition discussed above for the relaxation tests. Nevertheless, the predicted results are accurate in the range of use of this material model for building applications. However, it would be instrumental to integrate the developed model with a yield criterion and a viscoplastic model as part of future works.

The results of the additional 8-h creep tests performed at 0 °C and $\sigma_{creep} = 9$ MPa are reported in Fig. 11, showing an excellent agreement

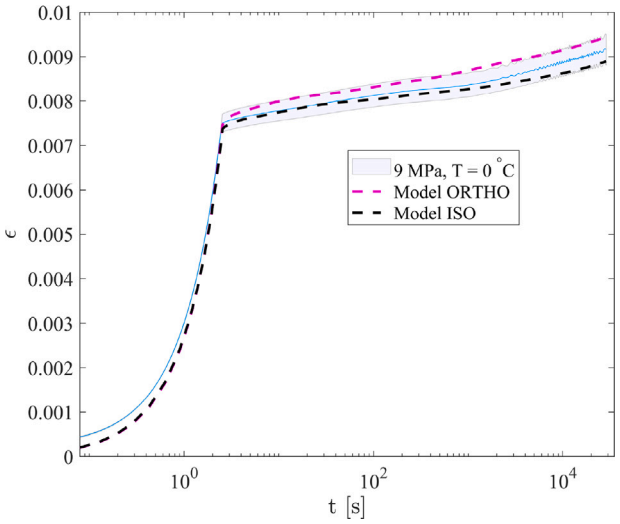

Fig. 11. Time strain evolution during an 8-h creep test at $\sigma_{creep} = 9$ MPa carried out at T = 0 °C along MD. The solid line represents the average experimental value, while the coloured area is the standard deviation. The dashed lines represent the FE simulations of a DMA rectangular specimen with the orthotropic (pink) and isotropic (black) models. (For interpretation of the references to colour in this figure legend, the reader is referred to the web version of this article.)

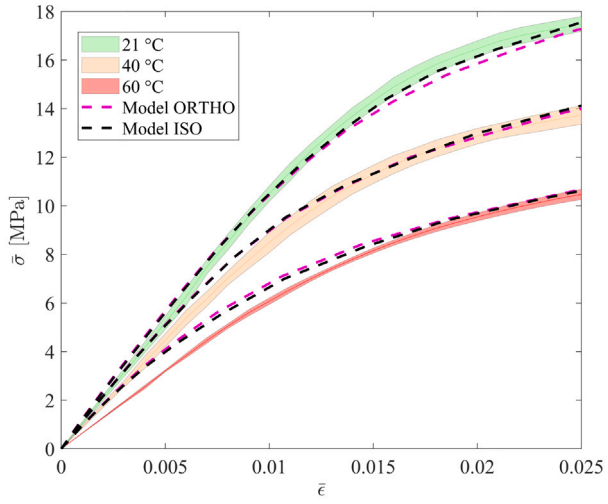

Fig. 12. Temperature effects on ETFE engineering equivalent stress–strain curves at 0.1%/s strain rate at the apex of circular inflation test. The solid line represents the average experimental value, while the coloured area is the standard deviation. The dashed lines represent the FE simulation of a circular inflated specimen with the orthotropic (pink) and isotropic (black) models. (For interpretation of the references to colour in this figure legend, the reader is referred to the web version of this article.)

between model predictions and measures. Both models can capture the strain at the end of the loading ramp and its evolution over time ($R^2 = 0.9992$ and $R^2 = 0.9987$ for the isotropic and orthotropic model, respectively).

4.5. Circular inflation tests

The model predictions of circular diaphragm tests were compared to the experimental data in terms of equivalent stress $\bar{\sigma}$ and strain $\bar{\epsilon}$ quantities extracted at the apex of each sample. The average error is around 5% and 3% for the orthotropic and isotropic models, respectively, testifying the excellent agreement shown in Fig. 12. The main differences arose in the tests at 60 °C, with a maximum error of 14.4% and 9.7% at the highest pressure rate for the orthotropic and isotropic

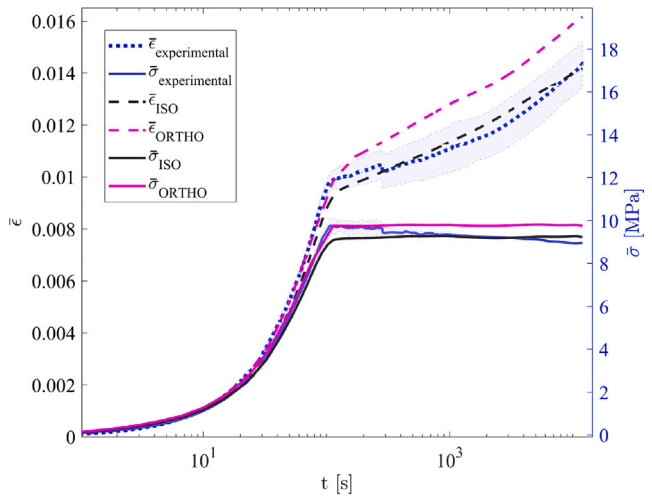

Fig. 13. ETFE engineering equivalent strain (left vertical axis) and equivalent stress (right vertical axis) vs. time during biaxial inflation creep test at T = 21 °C. The solid and dashed blue curves represent the average experimental stress and strain values, while the coloured area is the standard deviation. The solid and dashed lines represent the stress and strain from FE simulations of the orthotropic (pink) and isotropic (black) models. (For interpretation of the references to colour in this figure legend, the reader is referred to the web version of this article.)

models, respectively. At that temperature, it can be observed that the initial stiffness of the models, driven by the linear viscoelastic regime, is higher than the experimental data. Appendix C.2 reports additional plots of the circular inflation tests showing the effect of the pressure rate, which was found to be limited because the strain rate variation achieved was less pronounced than expected, as detailed in Table 2.

4.6. Circular creep inflation tests

The creep tests on pressurised circular samples, aimed to reach constant stress at the apex of the membrane, are presented as part of the validation of the model. As Fig. 13 depicts, the constitutive models developed correctly capture the time dependence of the strain evolution at the apex of the membrane when applying to the FE model the same pressure history of the experiments, with $R^2 = 0.9963$ and $R^2 = 0.9709$ for the isotropic and orthotropic models, respectively. This shows how both models can accurately predict the creep behaviour in a biaxial configuration as well as in the uniaxial condition presented in Section 4.4. It should be noted that performing creep conditions on an inflation setup is rather complex to fine-tune because the test is under pressure control, and it was not further investigated in this work.

4.7. Elliptical inflation tests

The elliptical inflation tests performed showed similar results in the stress–strain curves as the circular bulge tests; this was expected since the strain rates and temperature conditions were almost equivalent. The effect of temperature on the elliptical inflation tests at a strain rate of 0.1%/s is shown in Fig. 14 for MD (left) and TD (right). In particular, the average error between model prediction and experimental measurements is limited to 5.9% for the orthotropic model and 5.6% for the isotropic model. The highest discrepancy was recorded in the tests at 60 °C, confirming what observed for the circular tests in the same thermal condition. The predictions for the orthotropic model presented an 11.4% error, averaged between the MD and TD orientations, and the isotropic model reported a 13% error in MD orientation but only a 6.6% discrepancy in TD. The difference between the errors depending on the specimen orientation was further investigated by plotting the principal stresses at the apex separately, as shown in Figs. 15 to 18 for different inflation pressure rates and temperatures. It should be noted that in those figures, the colours of the experimental curves refer to the stress in the short (light blue colour) and long (light red colour) axis of the ellipse: the legend assigns it to either MD or TD, changing between the left and right plot of each figure.

It was possible to notice how, in the MD tests, where the extrusion direction is parallel to the short (or minor) axis of the ellipse, the orthotropic model shows a good agreement qualitatively, as confirmed by the errors reported above for the equivalent quantities. However, when TD is aligned with the short axis (labelled as TD test), there is a higher discrepancy than in the MD direction, amounting to an average of 20% of the stress. Overall, the isotropic formulation better predicted the stresses in both directions, resulting in a more accurate model to simulate the elliptical test behaviour. In fact, the results of the tests show a stress distribution closer to an isotropic material: the superposition of the MD and TD tests experimental curves, Fig. 19, confirmed it. The orthotropic model is not able to accurately predict one of the two configurations, as the inaccuracy of the material model is amplified by the stress distribution: the short-axis stresses seem to be less influenced by the material model than the stresses on the long axis.

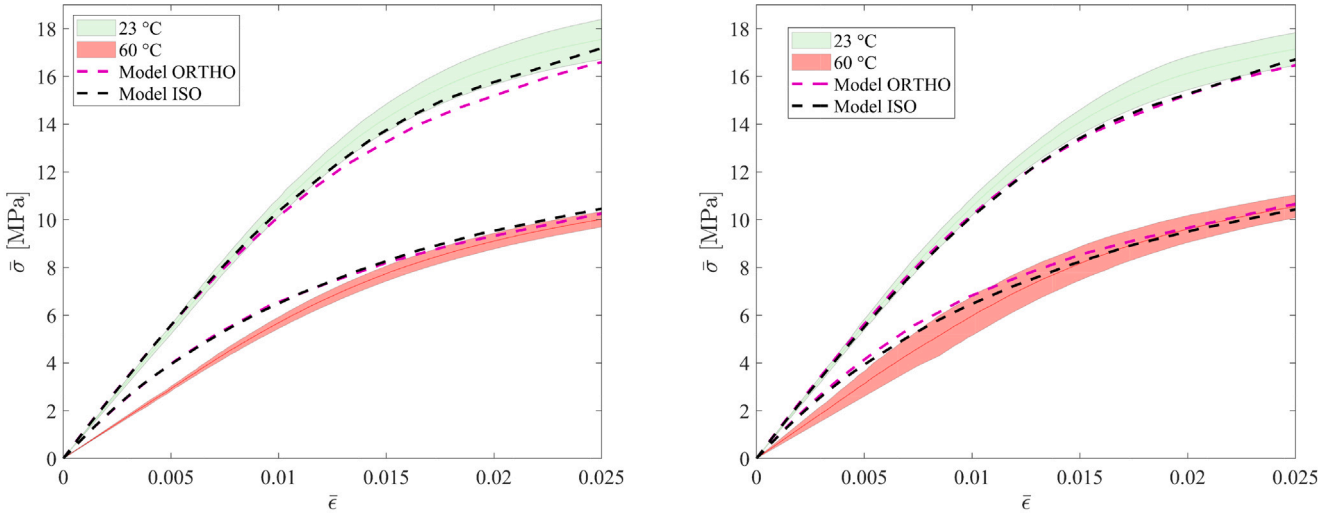

Fig. 14. ETFE equivalent engineering stress–strain curve for elliptical inflation tests performed at T = 23 °C and T =60 °C, for TD (left) and MD (right) aligned along the major axis of the elliptical sample. The pressure rate was 1200 Pa/s, resulting in a $\dot{\bar{\epsilon}} \approx 0.1\%/s$ strain rate at the apex of the sample. The solid line represents the average experimental values, while the coloured area is the standard deviation. The dashed lines represent the FE simulations obtained with orthotropic (pink) and isotropic (black) models. (For interpretation of the references to colour in this figure legend, the reader is referred to the web version of this article.)

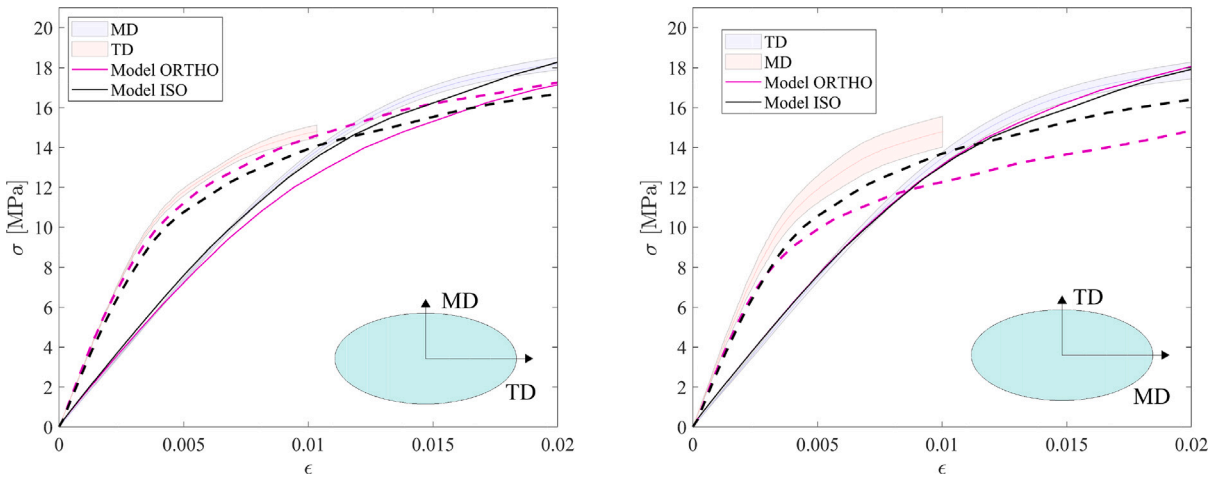

Fig. 15. ETFE engineering MD and TD stress–strain curves for elliptical inflation tests performed at T = 24.5 °C with a pressure rate of 300 Pa/s ($\dot{\bar{\epsilon}} \approx 0.02\%/s$ at the apex of the sample). The solid line represents the average experimental values, while the coloured area is the standard deviation. The solid and dashed lines represent the stresses along the minor and major ellipse axes from FE simulations obtained with orthotropic (pink) and isotropic (black) models. (For interpretation of the references to colour in this figure legend, the reader is referred to the web version of this article.)

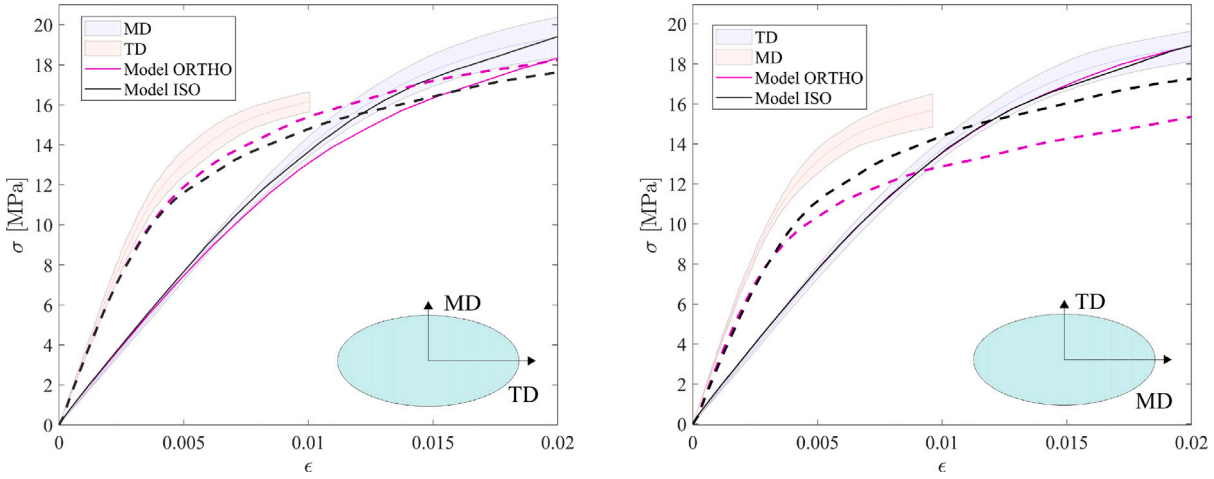

Fig. 16. ETFE engineering MD and TD stress–strain curves for elliptical inflation tests performed at T = 23 °C with a pressure rate of 1200 Pa/s ($\dot{\bar{\epsilon}} \approx 0.05\%/s$ at the apex of the sample). The solid line represents the average experimental values, while the coloured area is the standard deviation. The solid and dashed lines represent the stresses along the minor and major ellipse axes from FE simulations obtained with orthotropic (pink) and isotropic (black) models. (For interpretation of the references to colour in this figure legend, the reader is referred to the web version of this article.)

The elliptical inflation tests showed differences in the proposed models that were not apparent when comparing numerical predictions and experimental measurements from tensile or inflation tests, from which uniaxial or equibiaxial equivalent quantities were plotted. To further verify the accuracy of the two models when considering the directional quantities rather than the equivalent, the MD and TD stresses from circular inflation tests at T = 24 °C, $\dot{p}$ = 300Pa/s, are shown in Fig. 20.

The analysis of the circular test shows that the predictions of the orthotropic model are less accurate than the isotropic response, especially towards the yield stress. In particular, the MD principal quantities are the most discrepant, with an $R^2 = 0.9008$ compared to the experimental curve of the quantities in the same directions. At the same time, for TD, the prediction is accurate, as $R^2 = 0.9832$. In contrast, the isotropic model produced a response that closely resembled the calculated principal stresses and the simplified calculation used for the circular inflation tests of Section 4.5 ($R^2 = 0.971$ for both MD and TD directions).

A validation was also performed in the tests of Fig. 20, where contour plots were produced for the four principal quantities of interest (σ_{MD}, σ_{TD}, ϵ_{MD}, ϵ_{TD}), highlighted in the same figures with star markers. In particular, the experimental contours were obtained by displaying the strains of one single experiment, exported from the DIC experimental measurements, and the related stresses, calculated with FE and the developed models on the shape extracted from the DIC (method described in 2.1.3). The model contours were obtained by simulating the same experiment with equal boundaries and loading conditions. It is possible to notice that the points of extraction in Fig. 20 are not precisely aligned with the average curves reported. This happens for multiple reasons, such as the noise of the experimental data, the natural variation of the properties of the material across the specimen and the averaging adopted in the extraction of the quantities at the apex.

The contour plots of the circular tests are reported in Fig. 21, while those of elliptical tests in Figs. 22 and 23, all showing very good agreement between model prediction and experimental data. The contours confirm what was already discussed and quantified in this section, with the isotropic model predicting the behaviour of the material with more accuracy, especially comparing the stresses along TD direction as per Figs. 21(a) and 22(a).

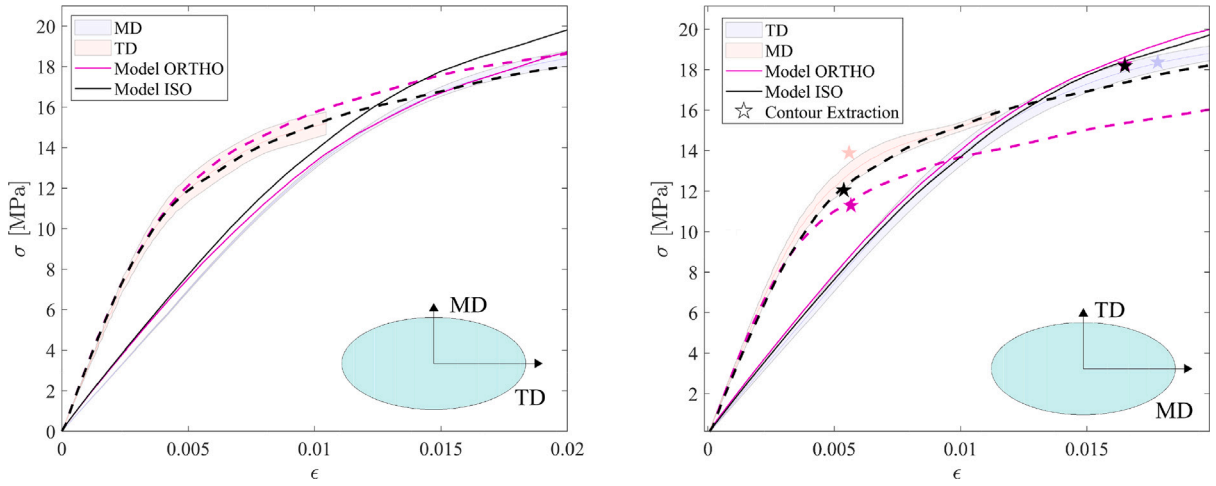

Fig. 17. ETFE engineering MD and TD stress–strain curves for elliptical inflation tests performed at T = 24 °C with a pressure rate of 2700 Pa/s ($\dot{\epsilon} \approx 0.2\%/s$ at the apex of the sample). The solid line represents the average experimental values, while the coloured area is the standard deviation. The solid and dashed lines represent the stresses along the minor and major ellipse axes from FE simulations obtained with orthotropic (pink) and isotropic (black) models. The star markers represent the instant of extraction of the field quantities of stress and strain in the contour plots of Figs. 22(a), 22(b), 23(a) and 23(b). (For interpretation of the references to colour in this figure legend, the reader is referred to the web version of this article.)

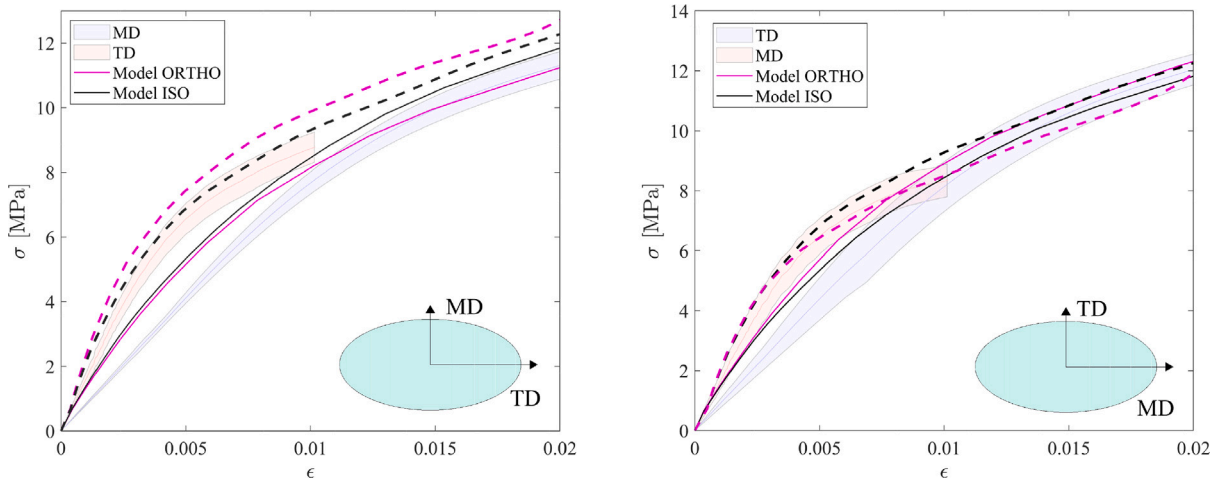

Fig. 18. ETFE engineering MD and TD stress–strain curves for elliptical inflation tests performed at T = 60 °C with a pressure rate of 1200 Pa/s ($\dot{\epsilon} \approx 0.1\%/s$ at the apex of the sample). The solid line represents the average experimental values, while the coloured area is the standard deviation. The solid and dashed lines represent the stresses along the minor and major ellipse axes from FE simulations obtained with orthotropic (pink) and isotropic (black) models. (For interpretation of the references to colour in this figure legend, the reader is referred to the web version of this article.)

5. Discussion

Two nonlinear viscoelastic models were proposed to describe and predict the response of a 200 μm-thick ETFE foil provided by one manufacturer, Nowofol. Overall, the accuracy of the models is very good in both formulations, although a higher overall accuracy across all the experiments carried out is achieved with the isotropic model, as shown in the previous section. Nevertheless, the orthotropic model showed a better agreement with tests carried out at lower temperatures. Moreover, the orthotropic formulation might be more useful in future developments, including the viscoplastic behaviour, which induces higher plasticity-induced orthotropic effects.

The development and implementation of comprehensive nonlinear viscoelastic models that can predict loading, cyclic, relaxation, and creep responses, both uniaxially and biaxially, are instrumental in the design of ETFE structures, which have gained popularity and are currently used in many engineering projects. These models can be utilised to monitor the time and temperature-dependent response of the foil in every stage of the construction process, from the pre-stressing phase at installation to the load cycles produced by wind or the creep caused by the snow load and the state of the foil after its removal. Given the lack of a design standard, the time effects related to these situations are currently overlooked or considered with simplified approaches in the design-supporting documents. For example, the TensiNet guidelines proposed a “long-term” elastic modulus and allowable stresses for permanent and long-term loads (see section A5.5 and A5.47, respectively, in [49]). The latter approach has been expanded to include more specific time definitions and temperatures in the FprCEN/TS 19102:2023 [25]; the former, however, has been abandoned and only a single value is available in the most recent contribution to ETFE structural design. To overcome the current simplified approach that might lead to an overdesign or unsafe design, the presented models provide a more refined design tool to evaluate ETFE behaviour beyond the conditions usually considered.

The developed models can be used in the temperature and strain rate ranges employed for the characterisation and validation of the constitutive law, i.e. temperatures spanning from −20 °C to 60 °C and strain rates from 10^{-5}%/s to 1%/s. Good extrapolation accuracy is not excluded outside the limits mentioned above, especially in the neighbouring region of these intervals. For time effects under creep and

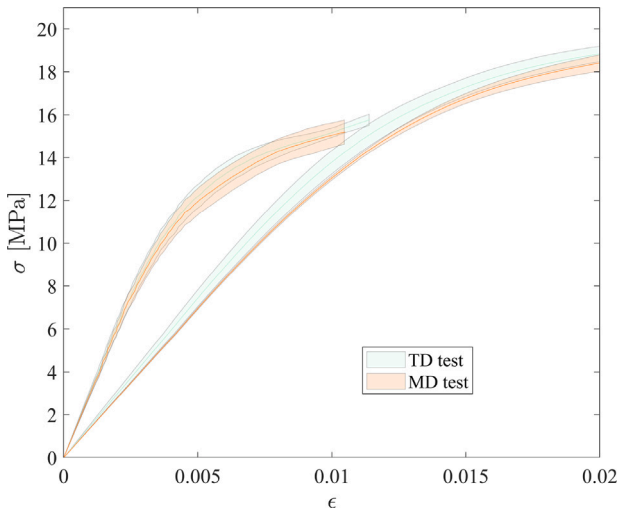

Fig. 19. Superposition of the ETFE engineering stress–strain curves on the long and short axis of the elliptical inflation tests performed at T = 24 °C with a pressure rate of 2700 Pa/s ($\dot{\hat{e}} \approx 0.2\%/s$ at the apex of the sample), obtained in the two orientations of the tests. TD and MD test in the legend represent the alignment of the material direction with the short axis of the ellipse. (For interpretation of the references to colour in this figure legend, the reader is referred to the web version of this article.)

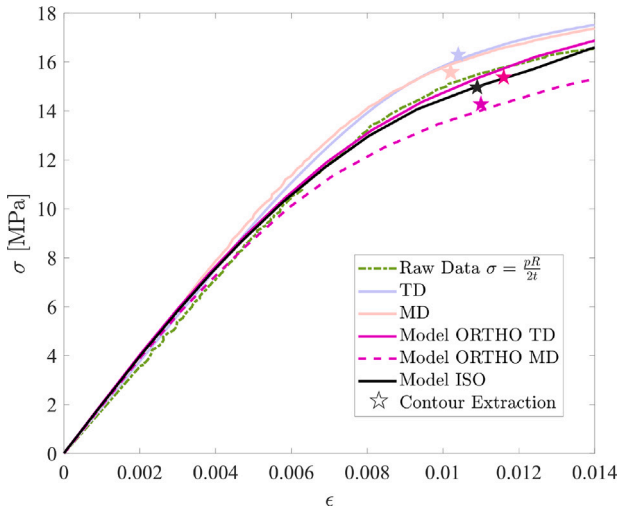

Fig. 20. ETFE engineering stress–strain curve during circular inflation tests at T = 24 °C and a pressure rate of 300 Pa/s. The first three items of the legend represent the experimental values MD and TD and the analytical formulation with material isotropy assumption (labelled as "Raw Data"). The predictions from FE simulations were obtained with orthotropic (pink, dashed and solid for MD and TD, respectively) and isotropic (black) constitutive models. The star markers represent the instant of extraction of the field quantities of stress and strain in the contour plots of Figs. 21(a)–21(d). The star markers do not lie exactly on the curve because they refer to one instant of only one experiment. The experimental markers differ because of the noise of the experimental data, the natural variation of the properties of the material across the specimen and the averaging adopted in the extraction of the quantities at the apex. The model markers differ because the curve is an average of the central elements of the FE simulation while the stars are specific values extracted from the contour. (For interpretation of the references to colour in this figure legend, the reader is referred to the web version of this article.)

relaxation, the models are expected to predict long-term loading conditions with good precision within the time limit of the master curves, despite the lack of such experimental validation for a very long time in this work. The limits of the master curves depend on the time, stress and thermal conditions. The higher the stress and the temperature, the shorter the maximum time-scale predictable: at constant ambient temperatures, the master curves can be used to predict the response for the entire designed life of the ETFE building, while at the isothermal condition of 60°, the time limit imposed by the master curves limits is on the order of several days, depending on mechanical loading. An additional limitation, significant for creep conditions, is that the model cannot predict the viscoplastic response. Hence, the limit is given by the onset of plasticity and the yield point. The proposed nonlinear viscoelastic models can provide accurate results until ca. 2–2.8% of equivalent strain, beyond which the onset of viscoplasticity occurs. Such limit was determined by identifying the strain at the first inflection point of stress–strain curves from uniaxial and biaxial tests performed at different temperatures and strain rates. However, a yield criterion that describes the evolution of yield locus with time and temperature effects and a viscoplastic model at finite strains will be developed to complement and integrate the present work [6,26]. From a design perspective for civil structures, this means that the models presented are mainly helpful for the Service Limit State (SLS), as in the Ultimate Limit State (ULS) ductile materials are allowed to reach the failure point; the restriction to the viscoelastic domain for such state can be very conservative. However, considering the load amplification factor of 1.5 between SLS and ULS in the EN 1990 [50] for variable loads (the main ones for building elements made of ETFE), and the high stress achieved by ETFE at failure, the SLS can be considered the most demanding design case. For example, the FprCEN/TS 19102:2023 [25] considers a limit stress for ETFE foils of 15 MPa for SLS and 40 MPa for ULS at $T = 23$ °C, stating that the ratio between the two limit stresses is higher than the load amplification factor, therefore confirming the SLS as more demanding in the design process.

Therefore, these models are foreseen to have a relevant impact on the design practice of ETFE membranes, both for inflated cushions and single-tensioned foils. For example, adopting these nonlinear viscoelastic models helps accurately predict the stress relaxation occurring during the installation of ETFE membranes in the prestressing phase, which the current design recommendations cannot predict. In a flat, tensioned single membrane, the initial stretch imposed on the material to reach the boundaries of a certain design geometry (e.g. a planar rectangle or a hypar) would cause a prestress, which inevitably relaxes over time. The installation procedure can be tuned to achieve a level of prestress sufficiently high to prevent (i) wind-induced fluttering and (ii) loss of relaxation due to thermal dilatation, at the same time avoiding excessive prestrains that could enhance the prestress loss due to relaxation. In the case of a cushion, the constant pressure between the foils causes creep, thus increasing strain over time. Moreover, it is necessary to maintain the resulting stresses within the yield domain, especially with temperature changes, snow loads, or cyclic wind loads. As an example, a temperature increase could result in plasticity onsetting on the most loaded parts of a cushion: the state of stress would be almost unaffected, as the shape modification would vary slightly and the pressure would not mutate, however, the yield surface would shrink relevantly.

Notwithstanding the advantages of the developed models, their limitations should be considered. First of all, during the experimental campaign, although only one type of foil from the same manufacturer (Nowofol ET6235Z) was used, the level of orthotropy between MD and TD over different batches of materials ranged between 5% and 20%. For this reason, when reduced orthotropy is measured or assumed, the isotropic model can be considered. Furthermore, different foil thicknesses (100 μm and 300 μm) of the same product type were tested in uniaxial conditions, at ambient temperature and at $\dot{\epsilon} = 0.1\%/s$. Some differences were found in the response compared with the reference thickness of 200 μm, mainly for the thinner foil (ca. -20% in the initial stiffness and ca. -40% in the yield stress). This effect was also documented by Surholt et al. [7] and De Focatiis and Gubler [4], who showed that the material manufacturer impacts the mechanical properties of ETFE. Therefore, the models developed here can be considered manufacturer and thickness-specific. However, the present work provides a viable procedure to build other reliable constitutive models for viscoelastic structural membranes, or the isotropic and orthotropic models presented can be factored into adapting to the ETFE response of different manufacturers or thicknesses.

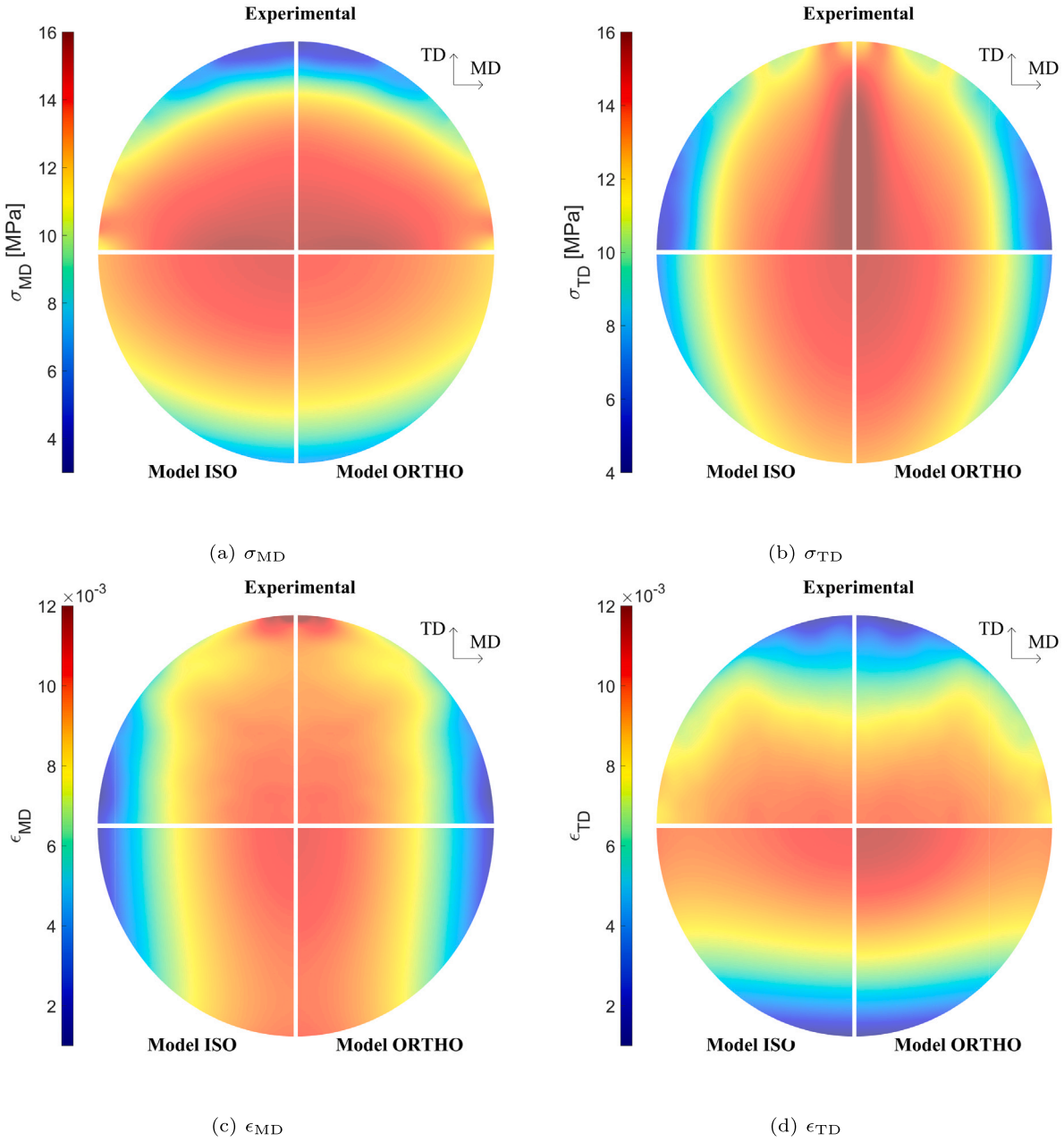

(a) σ_{MD} (b) σ_{TD}

(c) ϵ_{MD} (d) ϵ_{TD}

Fig. 21. Distribution of stresses (top) and strains (bottom) along MD and TD during a circular inflation test at T = 24 °C and $\dot{p}$ = 300 Pa/s ($\dot{\bar{\epsilon}} \approx 0.02\%/s$ at the apex of the membrane). The contour at the top of each quadrant represents the experimental data, while the ones at the bottom show the FE predictions using both the isotropic (left) and orthotropic (right) models. (For interpretation of the references to colour in this figure legend, the reader is referred to the web version of this article.)

6. Conclusion

ETFE thermomechanical characterisation and development of isotropic and orthotropic nonlinear viscoelastic constitutive models were presented in this work to accurately predict the material response in thermal, loading and strain rate ranges of typical building applications. The experimental campaign assessed several uniaxial and biaxial conditions, including tests not presented thus far in the literature, such as (i) relaxation tests at strain levels that approach the yield point, (ii) uniaxial and biaxial creep tests at different stress levels and their recovery to assess whether plasticity had developed, (iii) uniaxial cyclic tests in the nonlinear viscoelastic regime at different temperatures, (iv) circular and elliptical bulge experiments at constant pressure rates, with direct experimental stress determination, and (v) thermal expansion tests.

Leveraging on the comprehensive sets of experiments, one isotropic and one orthotropic nonlinear viscoelastic models were proposed and numerically implemented, based on the experimental creep compliance master curves obtained using the Time-Temperature Superposition principle (TTSP) to model the linear viscoelastic response and a stress shift factor according to the Eyring equation to model the material nonlinearities. Furthermore, a freezing of the stress shift factor was proposed to predict the unloading, cyclic and stress relaxation responses accurately. Both isotropic and orthotropic formulations achieved a high level of accuracy when compared with a set of independent tests (i.e. not used in the model fitting), although the isotopic model

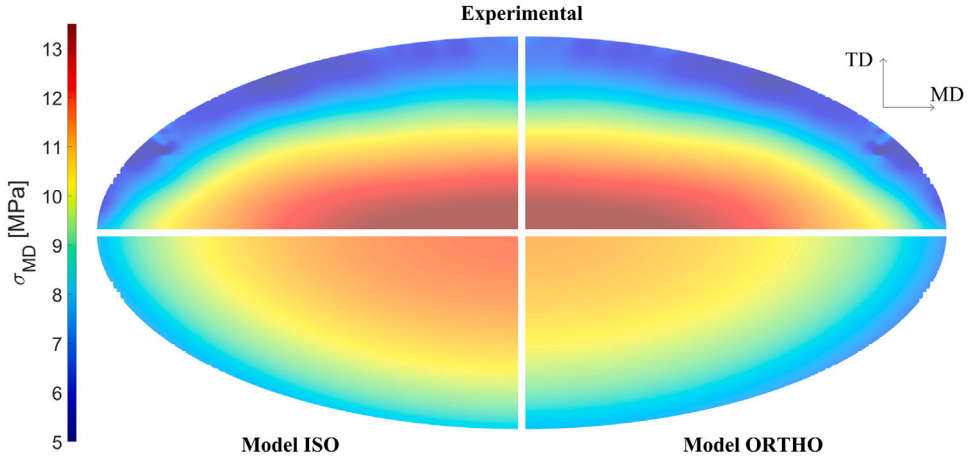

(a) σ_{MD}

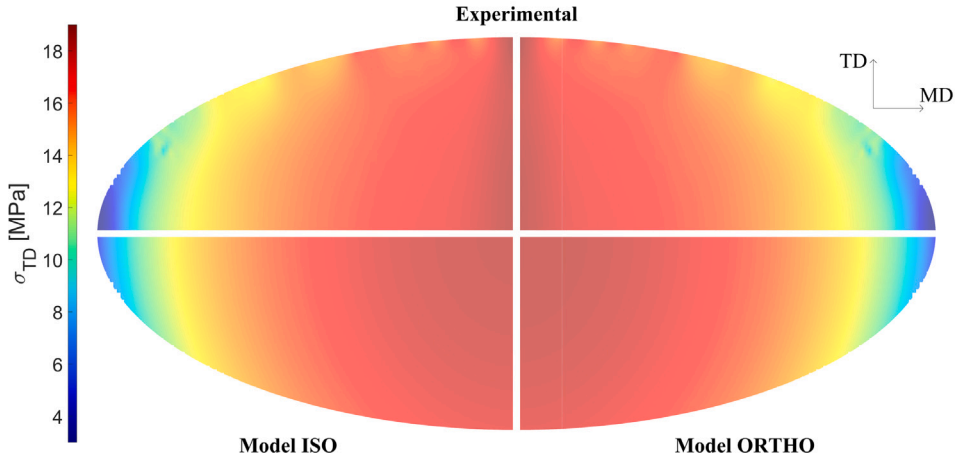

(b) σ_{TD}

Fig. 22. Distribution of stresses along MD (top) and TD (bottom) during an elliptical inflation test at T = 24 °C and $\dot{p}$ = 2700 Pa/s ($\dot{\varepsilon} \approx 0.2\%/s$ at the apex of the membrane). The contour at the top of each quadrant represents the experimental data, while the ones at the bottom show the FE predictions using both the isotropic (left) and orthotropic (right) models. (For interpretation of the references to colour in this figure legend, the reader is referred to the web version of this article.)

excelled in predicting principal stress states different from uniaxial or equibiaxial conditions. The models can predict ETFE response in a range of temperatures spanning from −20 °C to 60 °C and to timescales much more comprehensive than the laboratory times. The models are foreseen to impact ETFE structural design because they can reliably predict the material's time and temperature effects, prestress loss after installation, and creep response following a permanent load, such as snow and rain.

CRediT authorship contribution statement

Alessandro Comitti: Writing – review & editing, Writing – original draft, Validation, Software, Investigation, Formal analysis, Data curation. **Federico Bosi:** Writing – review & editing, Writing – original draft, Supervision, Resources, Project administration, Methodology, Funding acquisition, Conceptualization.

Declaration of competing interest

The authors declare that they have no known competing financial interests or personal relationships that could have appeared to influence the work reported in this paper.

Acknowledgements

The authors acknowledge support from the European Union through the project H2020-MSCA-ITN-2020-LIGHTEN-956547. Luis Seixas (CAEmate srl, UCL Mechanical Engineering), Adam Bown and Adrian Cabello (Tensys ltd) are also gratefully acknowledged for fruitful discussions. Luis Seixas is also acknowledged for performing some of the elliptical and creep inflation tests. Agustin Mengoni is acknowledged for his work on ETFE tests on different thicknesses. Phil Davies from TA Instrument is gratefully acknowledged for the execution of the thermal expansion tests.

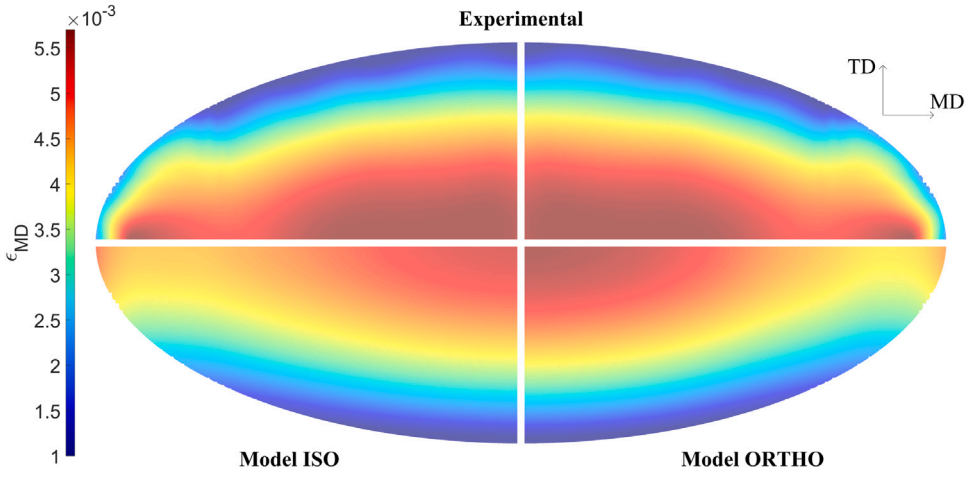

(a) ϵ_{MD}

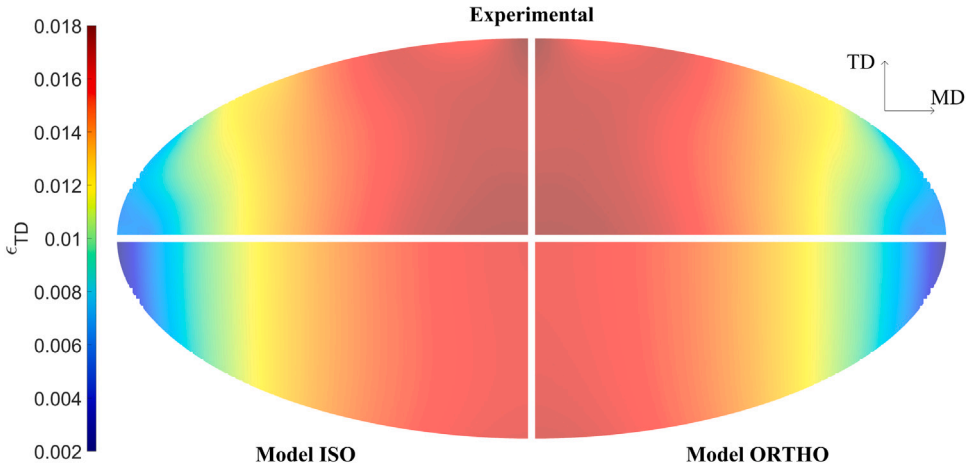

(b) ϵ_{TD}

Fig. 23. Distribution of strains along MD (top) and TD (bottom) during an elliptical inflation test at T = 24 °C and $\dot{p}$ = 2700 Pa/s ($\dot{\bar{\epsilon}} \approx 0.2\%$/s at the apex of the membrane). The contour at the top of each quadrant represents the experimental data, while the ones at the bottom show the FE predictions using both the isotropic (left) and orthotropic (right) models. (For interpretation of the references to colour in this figure legend, the reader is referred to the web version of this article.)

Appendix A. Creep compliance master curves and coefficients of thermal expansion

The material parameters determined for the creep compliance master curves are presented in Table A.5.

The MD, TD and ID directional creep compliance master curves are reported in Figs. A.24–A.26, respectively.

The thermal expansion coefficients used in the model are reported in Table A.6.

Appendix B. Biaxial inflation test setup and pressure profile

An illustration of the biaxial test rig is reported in Fig. B.27.

The pressure signal utilised for the biaxial creep tests is provided in Fig. B.28.

Appendix C. Additional results for the model validation

C.1. Uniaxial tensile tests

See Figs. C.29 and C.30.

C.2. Circular inflation tests

See Fig. C.31.

Data availability

The code of the developed nonlinear viscoelastic models and an example of its application can be found at github.com/fbosi/ETFE-NLVE-model. Additional data will be made available on request.

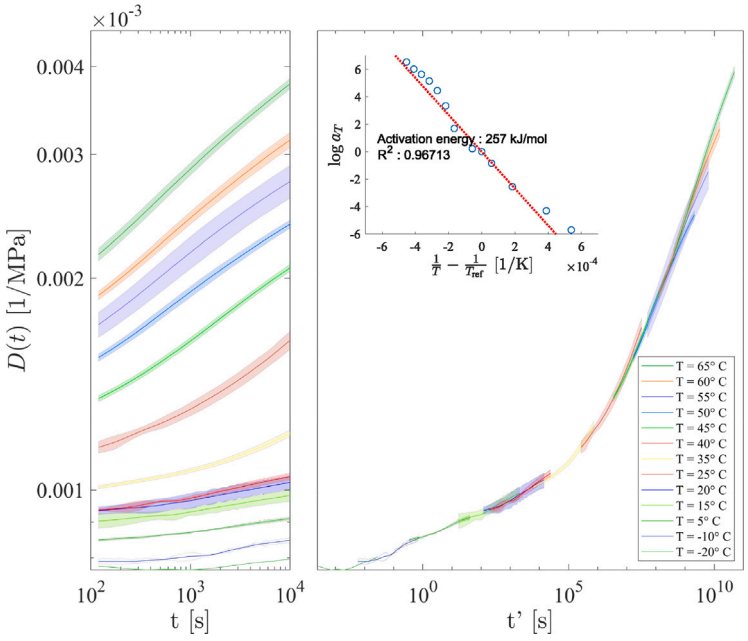

Fig. A.24. Left: engineering creep compliance at different temperatures from creep test performed at 1.5 MPa along MD. Right: Engineering creep compliance master curves along MD at T_{ref} = 20 °C, obtained by horizontally shifting the compliance curves at other temperatures through the time shift factor a_T. The inset shows the experimental shift factors and their fitting through the Arrhenius law. (For interpretation of the references to colour in this figure legend, the reader is referred to the web version of this article.)

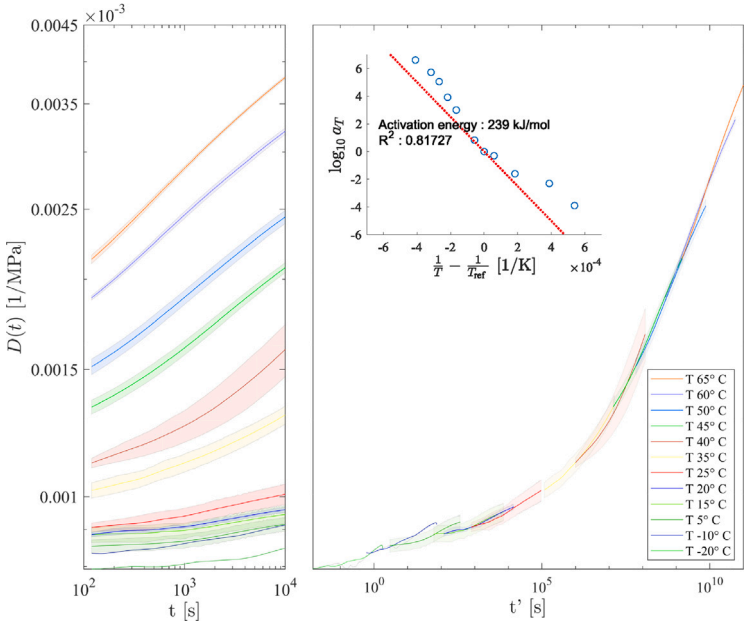

Fig. A.25. Left: engineering creep compliance at different temperatures from creep test performed at 1.5 MPa along TD. Right: Engineering creep compliance master curves along TD at T_{ref} = 20 °C, obtained by horizontally shifting the compliance curves at other temperatures through the time shift factor a_T. The inset shows the experimental shift factors and their fitting through the Arrhenius law. (For interpretation of the references to colour in this figure legend, the reader is referred to the web version of this article.)

Table A.5
Material parameters for ETFE creep compliance master curves.

	MD	TD	ID	
E_a [kJ/mol]	2.57E+05	2.39E+05	2.85E+05	2.73e+05
τ [s]	D_{11} [MPa]	D_{22} MPa	D_{66} [MPa]	D_{ISO} [MPa]
0.00E+00	5.33E−04	5.79E−04	8.75E−04	5.69E−04
1.00E−12	2.40E−05	1.98E−05	2.52E−05	2.14E−05
1.41E−11	2.41E−05	1.97E−05	2.49E−05	2.14E−05
2.00E−10	2.51E−05	2.03E−05	2.55E−05	2.21E−05
2.82E−09	2.62E−05	2.10E−05	2.63E−05	2.29E−05
3.98E−08	2.73E−05	2.18E−05	2.70E−05	2.37E−05
5.62E−07	2.85E−05	2.22E−05	2.78E−05	2.47E−05
7.94E−06	2.97E−05	2.38E−05	2.84E−05	2.53E−05
1.12E−04	3.12E−05	2.21E−05	2.95E−05	2.69E−05
1.58E−03	3.18E−05	2.93E−05	2.94E−05	2.60E−05
2.24E−02	3.53E−05	2.08E−05	3.29E−05	3.20E−05
3.16E−01	3.13E−05	2.84E−05	2.65E−05	2.18E−05
4.47E+00	4.55E−05	3.22E−05	4.21E−05	4.11E−05
6.31E+01	3.28E−05	2.40E−05	4.59E−05	2.65E−05
8.91E+02	5.34E−05	2.92E−05	5.57E−05	3.00E−05
1.26E+04	5.62E−05	6.06E−05	7.63E−05	7.50E−05
1.78E+05	1.14E−04	7.15E−05	1.04E−04	7.68E−05
2.51E+06	2.20E−04	1.54E−04	1.43E−04	2.56E−04
3.55E+07	3.61E−04	3.00E−04	3.92E−04	3.58E−04
5.01E+08	6.64E−04	5.00E−04	6.25E−04	6.53E−04
7.08E+09	1.01E−03	8.45E−04	1.06E−03	1.03E−03
1.00E+11	1.30E−03	1.38E−03	1.83E−03	1.23E−03

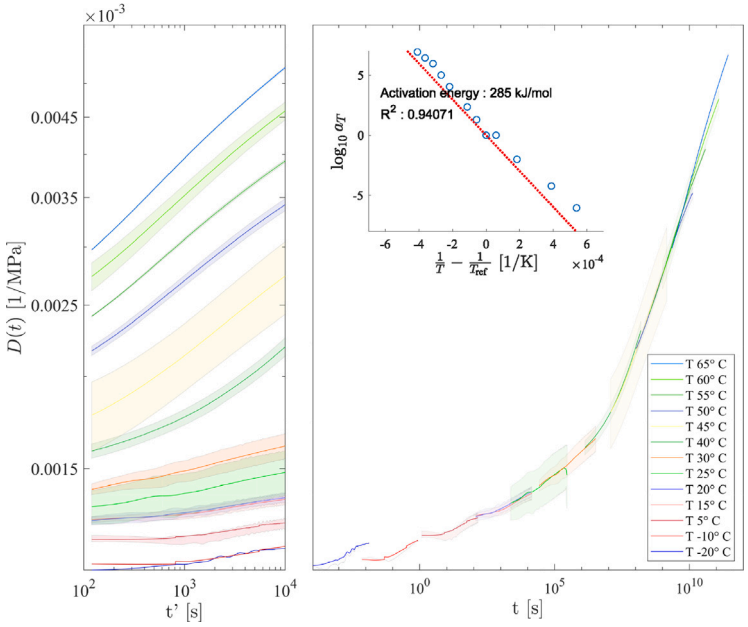

Fig. A.26. Left: engineering creep compliance at different temperatures from creep test performed at 0.75 MPa along ID. Right: Engineering creep compliance master curves along ID at T_{ref} = 20 °C, obtained by horizontally shifting the compliance curves at other temperatures through the time shift factor a_T. The inset shows the experimental shift factors and their fitting through the Arrhenius law. (For interpretation of the references to colour in this figure legend, the reader is referred to the web version of this article.)

Table A.6
Thermal expansion coefficients for ETFE.

j	MD	TD	Out of plane
	$p_j[K^{-1}]$		
6	−4.09066120158576E−14	−2.66353538597106E−14	0
5	6.90392747522749E−11	4.42294281889069E−11	0
4	−4.82586611176244E−08	−3.03716355455403E−08	0
3	1.78868578046235E−05	1.10404020141692E−05	0
2	−0.00370814669249724	−0.00224076695852706	0
1	0.407833614428186	0.240852471748044	0.000159136560773121
0	−18.6026514328471	−10.7202497929162	−0.0366732667349468

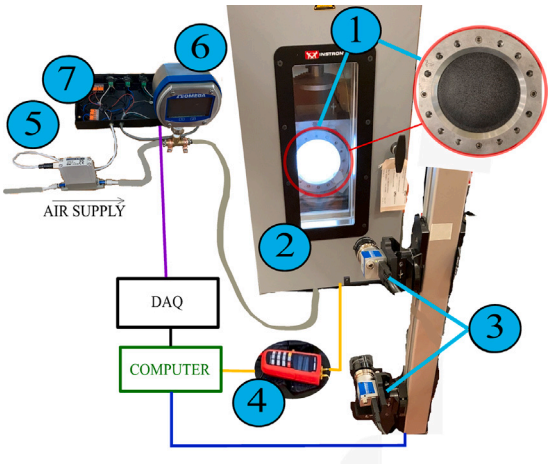

Fig. B.27. Biaxial inflation setup composed of a metallic box with an elliptical or circular cut on the lid, equipped with LED lights inside, where the specimen is clamped (1). The test box is placed inside an environmental chamber when thermal tests are performed (2). The stereo DIC cameras (3) and the temperature reader (4) record the kinematic field and the temperature of the specimen to the controlling computer, respectively. A pressure regulator (5) and a pressure gauge (6) are connected to a DAQ through a control circuit (7), which regulates the air inlet in the bulge test box. (For interpretation of the references to colour in this figure legend, the reader is referred to the web version of this article.)

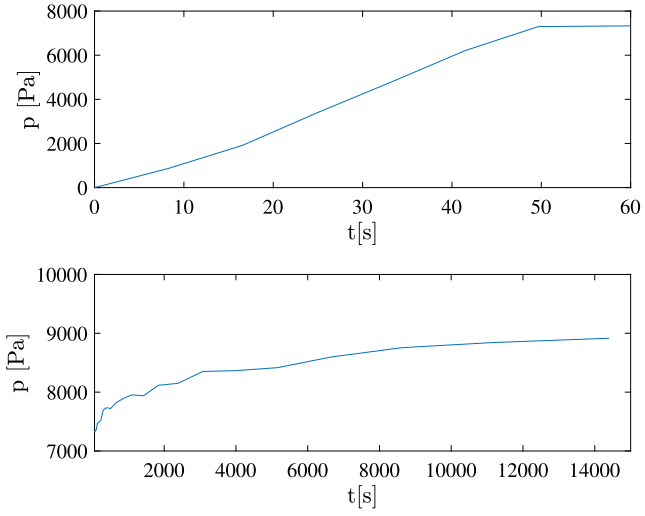

Fig. B.28. Pressure signal utilised for the biaxial creep inflation tests, comprehensive of the initial loading ramp at constant pressure rate (above) and the subsequent long-term creep phase (below). (For interpretation of the references to colour in this figure legend, the reader is referred to the web version of this article.)

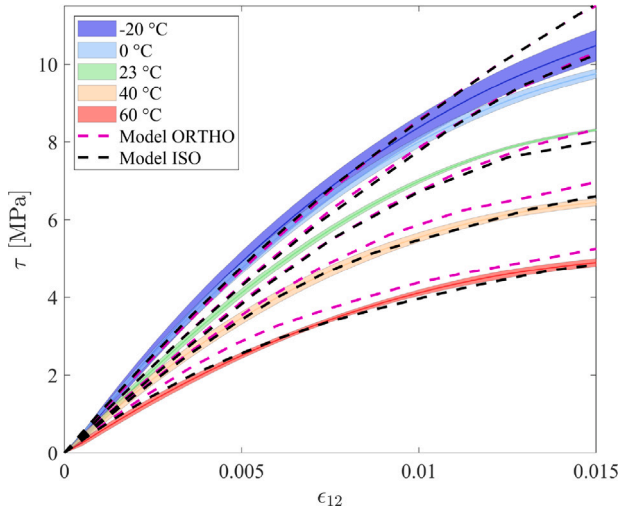

Fig. C.29. Temperature effects on ETFE engineering stress–strain curves at 0.1%/s strain rate along ID [5]. The solid line represents the average experimental value, while the coloured area is the standard deviation. The dashed lines represent the FE simulations of a dumbbell specimen with the orthotropic (pink) and isotropic (black) models. (For interpretation of the references to colour in this figure legend, the reader is referred to the web version of this article.)

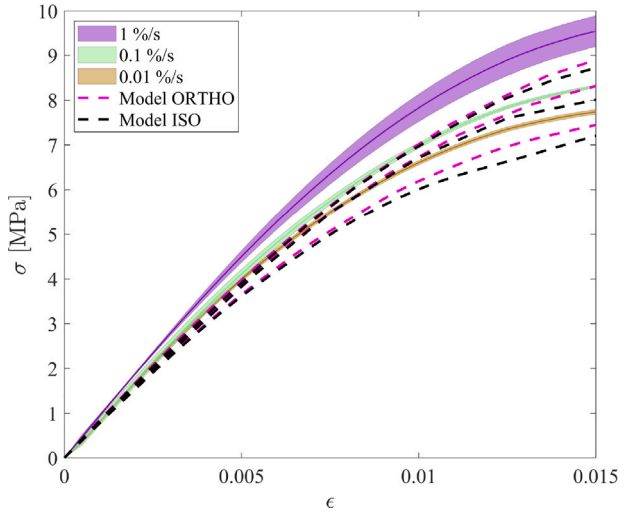

Fig. C.30. Strain rate effects on ETFE engineering stress–strain curve at T_{amb} = 23 °C and along ID [5]. The solid line represents the average experimental value, while the coloured area is the standard deviation. The dashed lines represent the FE simulations of a dumbbell specimen with the orthotropic (pink) and isotropic (black) models. (For interpretation of the references to colour in this figure legend, the reader is referred to the web version of this article.)

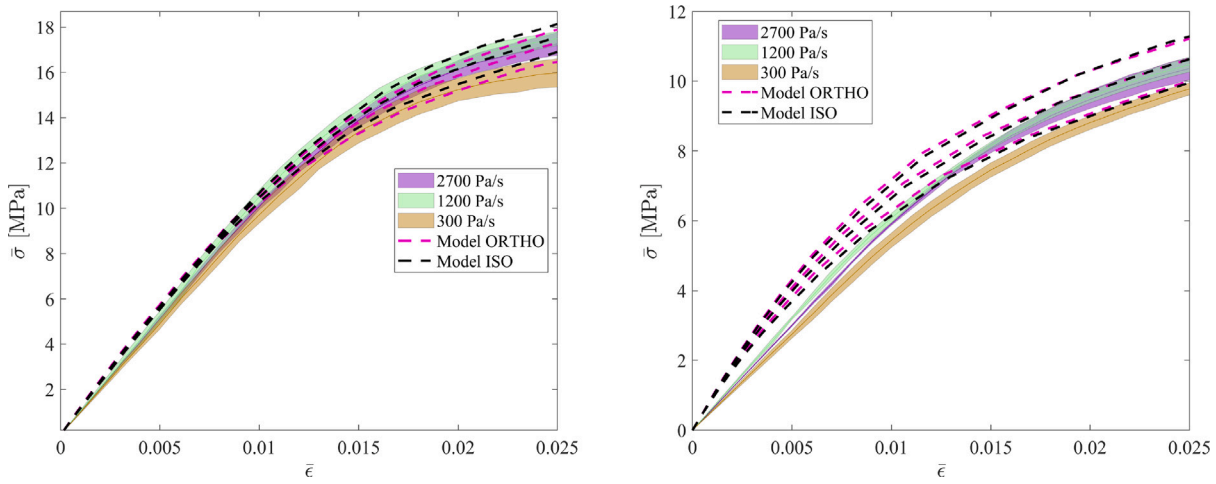

Fig. C.31. Pressure rate effects on ETFE engineering stress–strain curves from circular inflation test at $T = 23$ °C (left) and $T = 60$ °C (right). The solid line represents the average experimental value, while the coloured area is the standard deviation. The dashed lines represent the FE simulations of a circular inflated specimen with the orthotropic (pink) and isotropic (black) models. (For interpretation of the references to colour in this figure legend, the reader is referred to the web version of this article.)

References

[1] Jianhui Hu, Wujun Chen, Bing Zhao, Deqing Yang, Buildings with ETFE foils: A review on material properties, architectural performance and structural behavior, Constr. Build. Mater. (ISSN: 09500618) 131 (2017) 411–422.

[2] Alessandro Comitti, Harikrishnan Vijayakumaran, Mohammad Hosein Nejabatmeimandi, Luis Seixas, Adrian Cabello, Diego Misseroni, Massimo Penasa, Christoph Paech, Miguel Bessa, Adam C. Bown, Francesco Dal Corso, Federico Bosi, Ultralight membrane structures towards a sustainable environment, in: Sustainable Structures and Buildings, Springer, Nantes, 2023.

[3] Syreeta Robinson-Gayle, Maria Kolokotroni, Andrew Cripps, S Tanno, ETFE foil cushions in roofs and atria, Constr. Build. Mater. (ISSN: 09500618) 15 (7) (2001) 323–327.

[4] Davide S.A. De Focatiis, Lorenz Gubler, Uniaxial deformation and orientation of ethylene–tetrafluoroethylene films, Polym. Test. (ISSN: 01429418) 32 (8) (2013) 1423–1435.

[5] Alessandro Comitti, Federico Bosi, Thermomechanical characterisation and plane stress linear viscoelastic modelling of ethylene-tetra-fluoroethylene foils, Mech. Time-Depend. Mater. 59 (1) (2024) 25–45.

[6] Luis Seixas, Alessandro Comitti, Massimo Penasa, Federico Bosi, Characterisation and modelling of ETFE membranes for tensile structures, in: Proceedings of IASS 2024, International Association for Shell and Spatial Structures, Zurich, 2024.

[7] Felix Surholt, Jörg Uhlemann, Natalie Stranghöner, Temperature and strain rate effects on the uniaxial tensile behaviour of ETFE foils, Polymers (ISSN: 2073-4360) 14 (15) (2022) 3156.

[8] Cedric Galliot, Rolf H. Luchsinger, Uniaxial and biaxial mechanical properties of ETFE foils, Polym. Test. (ISSN: 01429418) 30 (4) (2011) 356–365.

[9] Jianhui Hu, Wujun Chen, Bing Zhao, Kai Wang, Uniaxial tensile mechanical properties and model parameters determination of ethylene tetrafluoroethylene (ETFE) foils, Constr. Build. Mater. (ISSN: 09500618) 75 (2015) 200–207.

[10] Felix Surholt, Jörg Uhlemann, Natalie Strangoener, Defining design limits for ETFE foils determined in bubble inflation tests, in: Proceedings of IASS Annual Symposia, Vol. 2023, International Association for Shell and Spatial Structures (IASS), Melbourne, 2023, pp. 1–12, 3.

[11] Yintang Li, Minger Wu, Uniaxial creep property and viscoelastic–plastic modelling of ethylene tetrafluoroethylene (ETFE) foil, Mech. Time-Depend. Mater. 19 (1) (2015) 21–34, issn: 1385-2000, 1573-2738.

[12] Linda Charbonneau, Maria Anna Polak, Alexander Penlidis, Mechanical properties of ETFE foils: Testing and modelling, Constr. Build. Mater. (ISSN: 09500618) 60 (2014) 63–72.

[13] Bing Zhao, Jianhui Hu, Wujun Chen, Jianwen Chen, Zhongliang Jing, Uniaxial tensile creep properties of ETFE foils at a wide range of loading stresses subjected to long-term loading, Constr. Build. Mater. (ISSN: 09500618) 253 (2020) 119112.

[14] Felix Surholt, Jörg Uhlemann, Natalie Strangoener, Correlation between uniaxial and biaxial creep behaviour of etfe foils, in: Proceedings of the XI International Conference on Textile Composites and Inflatable Structures, Vol. 2023, EUROMECH, Valencia, 2023, pp. 1–12, 3.

[15] Roland Lippke, Folien als Transparente Elemente in der Fassade. Mechanische und Bauphysikalische Eigenschaften (Ph.D. thesis), Technischen Universität Berlin, 2009.

[16] Christian Hartz, Luftdruckgesteuerte Transformation an flexibel berandeten Folienkissen (Ph.D. thesis), Technischen Universität Berlin, 2014.

[17] Klaus Saxe, Zur berechnung und bemessung von ETFE-folientragwerken, in: Proceedings of the Essener Membranbau Symposium, 2012.

[18] Tatuya Yoshino, Shiro Kato, Viscous characteristics of ETFE film sheet under temperature change in biaxial tensions, in: Proceedings of the IASS Symposium 2018, Boston, 2018, p. 8.

[19] Guojun Sun, Mingze Wu, Xiushu Qu, Suduo Xue, Experimental investigation of the uniaxial tensile properties and thermal deformation of the ETFE membrane at different temperatures, Constr. Build. Mater. (ISSN: 09500618) 327 (2022) 126944.

[20] Patrick Beck, Zum Zeit- Und Temperaturabhängigen Werkstoffverhalten Von Ethylen Tetrafluorethylen-Folien Im Hochbau (Ph.D. thesis), Technische Universität Darmstadt, 2021.

[21] Tatsuya Yoshino, Shiro Kato, Formulation of non-linear incremental constitutive equation of ETFE film structure considering the dependence on temperature change, in: Proceedings of the International Association for Shell and Spatial Structures (IASS) Symposium 2013, Wroclaw University of Technology, Poland, 2013, p. 5.

[22] Tatsuya Yoshino, Shiro Kato, Viscous characteristics of ETFE film sheet under equal biaxial tensions, Procedia Eng. (ISSN: 18777058) 155 (2016) 442–451.

[23] Tatsuya Yoshino, Shiro Kato, Viscous characteristics of ETFE film sheet under temperature change, in: VIII International Conference on Textile Composites and Inflatable Structures, Munich, 2017, p. 12.

[24] Tatsuya Yoshino, Shiro Kato, Viscous characteristics near the initial yield stress of ETFE film sheet under biaxial tension and temperature change, in: Proceedings of the IASS Annual Symposium 2019, Barcelona, 2019, p. 8.

[25] Natalie Stranghöner, Jörg Uhlemann, Faruk Bilginoglu, Kai-Uwe Bletzinger, Heidrun Bögner-Balz, Evi Corne, Nick Gibson, Peter Gosling, Rogier Houtman, Josep Llorens, Marc Malinowsky, Jean-Marc Marion, Marijke Mollaert, Meike Nieger, Giorgio Novati, Farid Sahnoune, Peter Siemens, Bernd Stimpfle, Vatyu Tanev, Jean-Christophe Thomas, Raposo De M. Do N. E S. De Sotto Mayor ML, Prospect for European Guidance for the Structural design of Tensile Membrane Structures, Tech. Rep. KJ-NA-31-430-EN-N (online),KJ-NA-31-430-EN-C (print), Publications Office of the European Union, Luxembourg (Luxembourg), 2023.

[26] Mohammad Hosein Nejabatmeimandi, Alessandro Comitti, Luis Seixas, Adrian Cabello, Adam Bown, Advancing the design of sustainable ETFE membrane structures: Insights from the lighten consortium project, in: Proceedings of the TensiNet Symposium 2023 TENSINANTES2023, Vol. 2023, TensiNet, Nantes, 2023, pp. 423–434.

[27] Michael A. Sutton, Jean Jose Orteu, Hubert Schreier, Image Correlation for Shape, Motion and Deformation Measurements: Basic Concepts, Theory and Applications, Springer Science & Business Media, ISBN: 978-0-387-78747-3, 2009.

[28] D11 Committee, Test Methods for Vulcanized Rubber and Thermoplastic ElastomersTension, Tech. Rep., ASTM International, 2021.

[29] Correlated Solutions, VIC-3D software manual, 2019.

[30] Khurram Suleman, Federico Bosi, Direct stress computations in arbitrarily shaped thin shells and elliptic bulge tests, Proc. R. Soc. A 478 (2268) (2022) 20220619.

[31] Hal F. Brinson, L. Catherine Brinson, Polymer Engineering Science and Viscoelasticity: an Introduction, Springer, New York, 2008, ISBN: 978-0-387-73860-4 978-0-387-73861-1, OCLC: ocn172979443.

[32] John Sweeney, Ian M. Ward, Mechanical Properties of Solid Polymers, John Wiley & Sons, 2013.

[33] Jun Li, Kawai Kwok, Sergio Pellegrino, Thermoviscoelastic models for polyethylene thin films, Mech. Time-Depend. Mater. 20 (2016) 13–43.

[34] Wesley Wong, Sergio Pellegrino, Wrinkled membranes I: experiments, J. Mech. Mater. Struct. 1 (1) (2006) 3–25.
[35] Richard A. Schapery, On the characterization of nonlinear viscoelastic materials, Polym. Eng. Sci. 9 (4) (1969) 295–310, issn: 0032-3888, 1548-2634.
[36] Junbiao Lai, A. Bakker, An integral constitutive equation for nonlinear plasto-viscoelastic behavior of high-density polyethylene, Polym. Eng. Sci. 35 (17) (1995) 1339–1347, issn: 0032-3888, 1548-2634.
[37] Wolfgang G. Knauss, Igor J. Emri, Non-linear viscoelasticity based on free volume consideration, in: Computational Methods in Nonlinear Structural and Solid Mechanics, Elsevier, ISBN: 978-0-08-027299-3, 1981, pp. 123–128.
[38] Henry Eyring, Viscosity, plasticity, and diffusion as examples of absolute reaction rates, J. Chem. Phys. 4 (4) (1936) 283–291, issn: 0021-9606, 1089-7690.
[39] Theo A. Tervoort, Edwin T.J. Klompen, Leon E. Govaert, A multi-mode approach to finite, three-dimensional, nonlinear viscoelastic behavior of polymer glasses, J. Rheol. 40 (5) (1996) 779–797, issn: 0148-6055, 1520-8516.
[40] Robert N. Haward, G. Thackray, The use of a mathematical model to describe isothermal stress-strain curves in glassy thermoplastics, Proc. R. Soc. Lond. Ser. A 302 (1471) (1968) 453–472, issn: 0080-4630, 2053-9169.
[41] Antonios Zacharatos, Evagelia Kontou, Nonlinear viscoelastic modeling of soft polymers, J. Appl. Polym. Sci. 132 (26) (2015).
[42] Gerassimos Spathis, Evi Kontou, Nonlinear viscoelastic model for the prediction of double yielding in a linear low-density polyethylene film, J. Appl. Polym. Sci. 91 (6) (2004) 3519–3527.
[43] Zihui Xia, Xinghe Shen, Fernand Ellyin, An assessment of nonlinearly viscoelastic constitutive models for cyclic loading: The effect of a general loading/unloading rule, Mech. Time-Depend. Mater. 9 (4) (2005) 79–98, issn: 1385-2000, 1573-2738.
[44] Federico Bosi, Sergio Pellegrino, Nonlinear thermomechanical response and constitutive modeling of viscoelastic polyethylene membranes, Mech. Mater. (ISSN: 01676636) 117 (2018) 9–21.
[45] Jinhe Chen, Minger Wu, Uniaxial tensile properties of pre-stretched ethylene-tetrafluoroethylene (ETFE) foil, Thin-Walled Struct. (ISSN: 0263-8231) 189 (2023) 110867.
[46] Masaya Kawabata, Structural behavior of circular air cushion considering variation of internal pressure and material plasticization, in: Proceedings of IASS Annual Symposia, vOL. 2019, International Association for Shell and Spatial Structures (IASS), 2019, pp. 1–8, 24.
[47] Donald G. Fesko, Nicholas W. Tschoegl, Time-temperature superposition in thermorheologically complex materials, J. Polym. Sci. C 35 (1) (2007) 51–69, issn: 04492994, 19353065.
[48] Khurram Suleman, Mechanics of Inflatable Membranes and Measurement of the Yield Domain in Soft Materials (Ph.D. thesis), UCL (University College London), 2023.
[49] Richard Houtman, TensiNet European Design Guide for Tensile Structures. Appendix 5: Design recommendations for ETFE foil structures, TensiNet Association, Brussel, 2013.
[50] CEN, EN 1990:Eurocode—Basis of structural design, 2002.